



Isocitrate dehydrogenase wt and IDHmut adult-type diffuse gliomas display distinct alterations in ribosome biogenesis and 2'O-methylation of ribosomal RNA

Hermes Paraqindes, Nour-El-Houda Mourksi, Samantha Ballesta, Jordan Hedjam, Fleur Bourdelais, Tanguy Fenouil, Thiébaud Picart, Frédéric Catez, Théo Combe, Anthony Ferrari, et al.

► To cite this version:

Hermes Paraqindes, Nour-El-Houda Mourksi, Samantha Ballesta, Jordan Hedjam, Fleur Bourdelais, et al.. Isocitrate dehydrogenase wt and IDHmut adult-type diffuse gliomas display distinct alterations in ribosome biogenesis and 2'O-methylation of ribosomal RNA. *Neuro-Oncology*, 2023, 10.1093/neuonc/noad140 . hal-04203242

HAL Id: hal-04203242

<https://hal.science/hal-04203242>

Submitted on 12 Oct 2023

HAL is a multi-disciplinary open access archive for the deposit and dissemination of scientific research documents, whether they are published or not. The documents may come from teaching and research institutions in France or abroad, or from public or private research centers.

L'archive ouverte pluridisciplinaire **HAL**, est destinée au dépôt et à la diffusion de documents scientifiques de niveau recherche, publiés ou non, émanant des établissements d'enseignement et de recherche français ou étrangers, des laboratoires publics ou privés.



Distributed under a Creative Commons Attribution 4.0 International License

IDHwt and IDHmut adult-type diffuse gliomas display distinct alterations in ribosome biogenesis and 2'O-methylation of ribosomal RNA

Hermes PARAQUINDES^{1,2,#}, Nour-EI-Houda MOURKSI^{1,#}, Samantha BALLESTA^{1,3,#}, Jordan HEDJAM¹, Fleur BOURDELAIS^{1,4}, Tanguy FENOUIL^{1,9}, Thiébaud PICART^{1,9}, Frédéric CATEZ¹, Théo COMBE^{1,2}, Anthony FERRARI^{1,2}, Janice KIELBASSA², Emilie THOMAS^{1,2}, Laurie TONON^{1,2}, Alain VIARI^{1,2,5}, Valéry ATTIGNON^{1,6}, Marjorie CARRE^{1,6}, Jessie PERROSSIER^{1,6}, Stéphane GIRAUD^{1,3}, Christophe VANBELLE^{1,12}, Mathieu GABUT¹, Danny BERGERON⁷, Michelle S SCOTT⁷, Luis CASTRO VEGA⁸, Nathalie MAGNE⁸, Emmanuelle HUILLARD⁸, Marc SANSON⁸, David MEYRONET^{1,9}, Jean-Jacques DIAZ¹, François DUCRAY^{1,11,*}, Virginie MARCEL^{1,#,*}, Sébastien DURAND^{1,#,*}

1. LabEx Dev2CAN, Institut Convergence Plascan, Centre de Recherche en Cancérologie de Lyon, Inserm U1052, CNRS UMR5286, Université de Lyon, Université Claude Bernard Lyon 1, Centre Léon Bérard, CEDEX 08, F-69373 Lyon, France

2. Synergie Lyon Cancer, Gilles Thomas Bioinformatics Platform, Centre Léon Bérard, CEDEX 08, F-69373 Lyon, France

3. Plateforme organoïdes 3D-ONCO, Université de Lyon, Université Claude Bernard Lyon 1, Inserm U1052, CNRS UMR5286, Centre Léon Bérard, Centre de Recherche en Cancérologie de Lyon (CRCL), Lyon, 69373, France

4. Inovarion, 75005, Paris, France.

5. INRIA Grenoble Rhône-Alpes, 38330 Montbonnot-Saint-Martin, France

6. Cancer Genomics Platform, Centre de Recherche en Cancérologie de Lyon, CEDEX 08, F-69373 Lyon, France

7. Département de biochimie et génomique fonctionnelle, Faculté de médecine et des sciences de la santé, Université de Sherbrooke, Sherbrooke, Québec J1E 4K8, Canada

8. Sorbonne Université, Inserm, CNRS, UMR51127, Institut du Cerveau, ICM, AP-HP, Hôpitaux Universitaires La Pitié Salpêtrière – Charles Foix, Service de Neurologie 2-Mazarin, 75013 Paris, France

9. Hospices Civils de Lyon, Laboratoire de biologie médicale et d'anatomie pathologique

10. Hospices Civils de Lyon, Service de Neurochirurgie tumorale et vasculaire, Hôpital
Pierre Wertheimer

11. Hospices Civils de Lyon, Service de neuro-oncologie, Hôpital Pierre Wertheimer

12. Plateforme d'Imagerie Cellulaire, Université de Lyon, Université Claude Bernard
Lyon 1, Inserm U1052, CNRS UMR5286, Centre Léon Bérard, Centre de Recherche
en Cancérologie de Lyon (CRCL), Lyon, 69373, France

Equal contribution as co-first or co-last authors

* Corresponding authors: francois.ducray@chu-lyon.fr, virginie.marcel@lyon.uni-
cancer.fr and sebastien.durand@inserm.fr

Keywords

glioma, IDH mutational status, ribosome, epitranscriptomics, ribosome biogenesis factors

Running title

Ribosome alterations in high-grade gliomas

Issue section

Basic and translational investigation

Key points (3)

- rRNA 2'Ome profiling distinguishes IDHwt and IDHmut adult-type diffuse gliomas
- Elevated expression of ribosome biogenesis factors is correlated with IDH mutational status
- High grade adult-type diffuse gliomas differentially respond to the RNA Pol I inhibitors BMH-21 and CX5461

Word count: 4991

Abstract

Background: High-grade adult-type diffuse gliomas (HGGs) constitute a heterogeneous group of aggressive tumors that are mostly incurable. Recent advances highlighting the contribution of ribosomes to cancer development have offered new clinical perspectives. Here, we uncovered that IDHwt and IDHmut HGGs display distinct alterations of ribosome biology, in terms of rRNA epitranscriptomics and ribosome biogenesis, which could constitute novel hallmarks that can be exploited for the management of these pathologies.

Methods: We analyzed (i) the ribosomal RNA 2'O-ribose methylation (rRNA 2'Ome) using RiboMethSeq and in-house developed bioinformatics tools (<https://github.com/RibosomeCRCL/ribomethseq-nf> and [rRMSAnalyzer](#)) on three independent cohorts compiling 71 HGGs (IDHwt n=30, IDHmut n=41) and 9 non-neoplastic samples, (ii) the expression of ribosome biogenesis factors using medium throughput RT-qPCR as a readout of ribosome biogenesis, and (iii) the sensitivity of 5 HGG cell lines to RNA Pol I inhibitors (CX5461, BMH21).

Results: Unsupervised analysis demonstrated that HGGs could be distinguished based on their rRNA 2'Ome epitranscriptomic profile, with IDHwt glioblastomas displaying the most significant alterations of rRNA 2'Ome at specific sites. In contrast, IDHmut HGGs are largely characterized by an overexpression of ribosome biogenesis factors compared to non-neoplastic tissues or IDHwt glioblastomas. Finally, IDHmut HGG-derived spheroids display higher cytotoxicity to CX5461 than IDHwt glioblastoma, while all HGG spheroids display a similar cytotoxicity to BMH-21.

Conclusion: In HGGs, IDH mutational status is associated with specific alterations of the ribosome biology and with distinct sensitivities to RNA Pol I inhibitors.

Importance of the study (146 words)

Consistent multi-omics studies have shown that high-grade adult-type diffuse gliomas (HGGs) can be classified into three main groups, *i.e.*, IDHmut and 1p/19q codeleted oligodendrogliomas, IDHmut astrocytomas and IDHwt glioblastomas, based on their genetic, transcriptomic and DNA methylation profiles. Recent advances have highlighted the contribution of ribosomes to cancer development and have offered new clinical perspectives. **Herein, we show that ribosomal RNA (rRNA) epitranscriptomic and ribosome biogenesis are different in distinct HGG types. We uncovered that IDHwt glioblastomas display the most prominent defects in rRNA epitranscriptomics, whereas IDHmut astrocytomas and oligodendrogliomas exhibit enhanced expression of ribosome biogenesis factors compared to IDHwt glioblastomas.** Moreover, based on their IDH mutational status, HGG-derived cell lines displayed distinct responses to CX5461 and BMH-21, two clinically-evaluated inhibitors of the RNA Pol I that transcribes rDNAs. This study identifies a connection between HGG oncogenesis and the ribosome biology, and highlights new therapeutic strategies.

Introduction

High-grade adult-type diffuse gliomas (HGGs) are brain tumors resembling glial cells that display highly heterogeneous prognoses and treatment responses. HGGs comprise three main histomolecular types, astrocytomas, oligodendrogliomas and glioblastomas, based notably on the mutational status of *isocitrate dehydrogenase (IDH)* 1 and 2^{1,2}. Indeed, glioblastomas are IDHwt, whereas astrocytomas and oligodendrogliomas are IDHmut, and can be further discriminated by the heterozygous 1p19q co-deletion occurring in oligodendrogliomas. IDHwt and IDHmut HGGs are associated with distinct epigenetic and transcriptomic dysregulations, leading to cancer-specific features. Thus, despite important advances in their histomolecular classification and understanding of their oncogenesis, HGGs remain mostly incurable. For instance, grade 4 IDHwt glioblastoma patients treated with the conventional combination of surgery, radiotherapy and temozolomide (TMZ) chemotherapy, display a median survival of only 15 months. Grade 3 IDHmut astrocytoma and oligodendroglioma patients treated with radiotherapy and chemotherapy exhibit a much better outcome with a median survival of 10 and 15 years, respectively, nevertheless 20 to 30% of the patients die within the first five years after diagnosis^{3,4}. Therefore, the identification of novel molecular mechanisms dysregulated in distinct HGG histomolecular types may significantly improve current therapeutic options.

Several studies highlighted that ribosome biogenesis (RiBi) and functions are altered in cancer cells and that ribosomes can support oncogenic functions⁵. For instance, the c-MYC oncogenic activity is in part supported by a dysregulation of genes implicated in RiBi and global protein synthesis⁶. In addition, levels of RiBi are generally increased in cancer cells to support the high protein synthesis demand caused by their exacerbated proliferation rate^{7,8} and therefore, the inhibition of rRNA synthesis specifically kills cancer cells without affecting normal cells^{9,10}. Such observations led to the development of molecules specifically inhibiting RiBi that showed objective responses in clinical trials, such as CX5461^{11–13}.

In addition to alteration of RiBi, recent observations suggest that variations of ribosome composition could also occur in cancer and be involved in disease etiology^{14–16}. The ribosome is composed of 80 ribosomal proteins and 4 ribosomal RNAs (rRNAs), the latter supporting the enzymatic activity of the peptidyl-bond formation during the translation of mRNAs into proteins. For many decades, the ribosome was considered as a monolithic entity displaying a similar composition in all cells constituting an organism.

However, it appears now that the ribosome composition can display some degree of variations, both at the level of ribosomal proteins and rRNA chemical modifications, which contributes to modulate intrinsic translational activities that could shape particular phenotypes^{17,18}. Variations of the ribosome composition at ribosomal protein levels have been reported in HGGs^{19–22}. In IDHwt glioblastomas, the overexpression of the ribosomal protein RPS6 was shown to promote acquisition of glioma stem cell properties, a hallmark of the most aggressive IDHwt glioblastomas^{20–22}. In addition, RPL22L1 isoforms are expressed in distinct regions of IDHwt glioblastomas through alternative splicing and induce the production of ribosomes with specific compositions, which promote translational bias towards specific mRNA subsets^{15,19,23–30}. In addition to ribosomal proteins, the chemical modifications of rRNA represent one of the major contributors to ribosome heterogeneity and led to the emergence of the notion of rRNA epitranscriptomics¹⁵. One of the main modifications, the methylation of the rRNA 2'O-ribose (rRNA 2'Ome), occurs at 106 known rRNA sites in humans and the 2'Ome at specific positions are essential for rRNA activity. The catalysis of rRNA 2'Ome is performed by an rRNA methylation complex composed of the methyl-transferase fibrillarin (FBL) and a single non-coding C/D box small nucleolar RNA (snoRNA or snoRD), which guides FBL at specific sites by base-pairing¹⁵. Hence, modulations of *FBL* or snoRD expression are sufficient to affect rRNA 2'Ome^{23,24,26}. Interestingly, alterations of 2'Ome have been observed in cancer and we recently demonstrated by profiling 195 primary mammary tumors using the RiboMethSeq approach, that only 40% of the known 2'O-methylated sites are altered, suggesting that only few rRNA sites can tolerate a lack of 2'Ome. Moreover, rRNA 2'Ome alterations are not random since rRNA 2'Ome profiles were associated with breast cancer subtypes and tumor grades²⁵. Similarly, alterations of rRNA 2'Ome were described in a cohort of 17 diffuse large B-cell lymphoma samples²⁷ and of 94 acute myeloid leukemia samples²⁸. Importantly, alterations of rRNA 2'Ome at some specific sites can affect both the translation of particular mRNA subsets and cell proliferation^{15,23,24,26 29,30}. To date, whether alterations of rRNA epitranscriptomics occurs in gliomas and contributes to disease etiology remains unexplored. Here, we investigated whether IDHwt and IDHmut HGGs display alterations in ribosome biology, in terms of rRNA epitranscriptomics and ribosome biogenesis, to exploit these features as novel therapeutic targets of these diseases.

Materials and methods

Human grade 3-4 adult-type diffuse glioma and non-neoplastic samples

Three cohorts were built: a technical cohort (8 grade 4 IDHwt glioblastomas, 3 non-tumoral samples); a test cohort detailed in Table 1 (13 IDHwt glioblastomas, 13 IDHmut astrocytomas, 14 IDHmut and 1p/19q codeleted oligodendrogliomas, 6 non-tumoral samples); a validation cohort (9 IDHwt glioblastomas, 6 IDHmut astrocytomas, 8 IDHmut and 1p/19q co-deleted oligodendrogliomas). The percentage of tumoral cells was estimated by a neuropathologist as described in Fig.S1. Additional details are provided in Supplementary Information.

Cell culture

Human IDHwt glioblastoma (5706, N131520), IDHmut astrocytoma (LGG85) and IDHmut and 1p/19q codeleted oligodendroglioma (BT138, BT237) cells were cultured as spheres as described in Supplementary Information.

Reverse Transcription and real time quantitative PCR

cDNA synthesis was performed using the Prime Script RT Reagent kit (Takara). Medium throughput qPCR was performed using the Biomark HD system (Fluidigm) as previously described³¹ (Table S1). The median Ct value of 5 housekeeping mRNAs was used for normalization.

RiboMethSeq

RiboMeth-seq was performed as previously described using the Illumina sequencing technology^{25,32}. To process the sequencing data, a novel nextflow pipeline RiboMethSeq-nf was developed and is currently available (<https://github.com/RibosomeCRCL/ribomethseq-nf>). This pipeline processes sequencing data as previously described^{25,32,33}. To calculate the C-score, which reflects the rRNA 2'Ome level, the novel R package rRMSAnalyzer was developed (<https://github.com/RibosomeCRCL/rRMSAnalyzer>). The identification of significant alterations in rRNA 2'Ome levels between groups was performed by applying two consecutive thresholds: the adjusted p-value < 0.05 (Kruskal-Wallis with FDR adjustment); and the mean Δ C-score (*i.e.*, difference between the highest and lowest mean C-score of the groups of interest) > 0.05.

IC₅₀ assay

3.10³ cell spheroids were treated with CX5461 (Sigma-Aldrich)³⁴ or BMH-21 (Sigma-Aldrich)¹⁰. Cell cytotoxicity was assessed by CellTox™ Green Cytotoxicity Assay (Promega) and by CellTiter-Glo3D® luminescent cell viability assay (Promega). Cell viability was expressed as a percentage of the signal intensity normalized against DMSO (1%).

Results

A standardized approach for large-scale analyses of human samples using RiboMethSeq

Before investigating alterations of rRNA 2'Ome in the three main histomolecular HGGs, we first optimized the recently described RiboMethSeq approach^{25,32,35} to determine reliable quantifications of 2'Ome levels at 106 rRNA sites from patient tumor samples. First, based on **the technical** cohort (n=11) of IDHwt glioblastomas and non-neoplastic tissues, we observed that the C-score, which reflects rRNA 2'Ome levels at specific sites, was similar using either a manual or an automated RNA extraction protocol (Fig.S2). Second, we used the NovaSeq Illumina sequencing platform (up to 10 billion reads) to increase the total number of **useful** reads (Fig.S3A) and the number of samples sequenced in a single flowcell.

We then randomly separated RNA samples of **the test** cohort and prepared two independent libraries of 23 samples (40 HGGs and 6 non-neoplastic samples), each library also contained a commercially-available “reference” total RNA. Unsupervised analysis of the entire **test** cohort using PCA based on C-scores of either all rRNA positions (7055 sites) or the 106 positions corresponding to known rRNA 2'Ome sites, clearly distinguished samples depending on the library of origin, as illustrated by the lack of clustering of reference RNA (**Fig. S3B, left panels**). We evaluated adjustment of RiboMethSeq data using the ComBat-seq algorithm, one of the most routinely used tools to adjust RNA-seq data³⁶. Upon ComBat-seq adjustment, no distinction between samples based on their library of origin was observed in C-scores, **including for the two reference RNA (Fig.S3B, right panels)**. These data demonstrate the efficacy of the ComBat-seq algorithm at removing batch effect from RiboMethSeq data.

Based on these results, we developed bioinformatics tools to perform reproducible analyses of RiboMethSeq data arising from large-scale cohorts (<https://github.com/RibosomeCRCL>).

rRNA 2'Ome profiles discriminate IDHwt from IDHmut adult-type diffuse gliomas

Using the optimized approach selected above, we then investigated whether alterations of rRNA 2'Ome differentially occur in the three main histomolecular HGGs **using the test cohort**: IDHwt glioblastoma (G, n=13), IDHmut astrocytoma (A, n=13), IDHmut and 1p19q codeleted oligodendroglioma (O, n=14) and non-neoplastic cerebral cortex (NT, n=6) (Table 1). Using unsupervised hierarchical clustering analysis (HCA), we first evaluated rRNA 2'Ome levels at the 106 known sites in the 46 non-neoplastic and glioma samples (Fig.1). The C-score reflects the rRNA 2'Ome levels as it corresponds to the ratio of the 5' read-end counts at a nucleotide position to the local 5' read-end count coverage; and when close to 1, C-score indicates that all rRNA molecules of the sample are 2'O-methylated at this specific site; whereas a C-score below 0.9 reflects a mix of 2'O-unmethylated and 2'O-methylated rRNA molecules. Here, most rRNA 2'Ome sites had a score close to 1, albeit some sites were below 0.9, substantiating recent results in human samples from diffuse large B cell lymphoma, acute myeloid leukemia and breast cancer^{25,27,28}. These data further confirmed observations by us and others that some rRNA molecules exist without 2'Ome at some specific sites, including in non-neoplastic tissue.

Interestingly, all IDHwt glioblastoma samples formed a separate branch (left-hand side of the HCA dendrogram), suggesting that their rRNA 2'Ome profile was clearly different from IDHmut astrocytoma and oligodendroglioma, as well as from non-neoplastic tissue (Fig.1). Principal Component Analyses (PCAs) based on the rRNA 2'Ome profile indicated that the PC2 axis (variance=14.1%) strongly differentiated glioblastomas from other samples (Fig.S4A). **To ensure consistency between the results of our classification and the expected outcome of the patients, we correlated PCA axes with survivals and mitotic index, as an internal control of tumor sample classification. Consistent with the known differences regarding glioblastomas and IDHmt HGGs characteristics, PC2 was significantly correlated with the *IDH1/2* mutational status, the mitotic index, overall survival (OS) and progression-free survival (PFS) (Fig.S4B-D). To validate these observations, we analyzed rRNA 2'Ome levels using RiboMethSeq on the**

technical cohort, corresponding to an independent cohort composed of 8 IDHwt glioblastomas and 3 non-neoplastic tissues. Unsupervised PCA based on the rRNA 2'Ome profile showed that IDHwt glioblastomas could once again be clearly separated from non-neoplastic tissues (Fig.S4E). Altogether, our data revealed that rRNA 2'Ome levels vary in HGGs as well as in non-neoplastic cerebral cortex, and that rRNA 2'Ome profiles discriminate IDHwt glioblastomas not only from non-neoplastic tissues but also from IDHmut HGG types.

Most variable rRNA 2'Ome sites are sufficient to discriminate IDHwt glioblastoma from IDHmut adult-type diffuse gliomas

To better characterize differences in rRNA 2'Ome profiles between histomolecular HGG types, we then focused on the most variable rRNA 2'Ome sites. To identify such sites, we compared the variability of C-scores at each single site among all HGG samples of the test cohort (n=40) using the distribution of the inter-quartile range (IQR). A set of 19 sites showed an IQR higher than median + 2 × median absolute deviation (mad) and were considered as the most variable rRNA 2'Ome sites among HGGs (red, Fig.2A), in agreement with our recent findings that only a subset of rRNA sites displays variability in 2'Ome levels²⁵. Interestingly, PCAs indicated that rRNA 2'Ome profiles based on this set of 19 sites are sufficient to discriminate IDHwt glioblastomas, IDHmut astrocytoma and oligodendrogliomas (Fig.2B).

To validate these observations, we used a second, independent validation cohort of 23 HGG samples (9 IDHwt glioblastomas, 6 IDHmut astrocytomas and 8 IDHmut, 1p/19q codeleted oligodendrogliomas) (Fig.S1B). We performed an unsupervised analysis using the 19 most variable rRNA 2'Ome sites identified using the test cohort (Fig.2A). As for the test cohort, unsupervised analyses of the validation cohort distinguished the three histomolecular subtypes of HGGs (Fig.2C). In addition, the projection of the validation cohort samples onto the PCA constructed from the test cohort enabled us to identify the histomolecular subtypes of each sample, suggesting that *de novo* profiling of rRNA 2'Ome could help in the classification of HGGs (Fig.2D). In addition, comparison of test and validation cohorts in term of percentage of tumor cells suggests that the tumor heterogeneity did not affect our conclusions (Fig. S1B). Indeed, in the validation cohort, the mean percentage of tumor cells is significantly lower in astrocytomas (38%) compared to oligodendrogliomas (69%), while no difference was observed with glioblastomas (9%) (Kruskal-Wallis: p=0.045*; Mann-Whitney: A vs O

p=0.024*). In contrast, in the test cohort, the mean percentage of tumor cells is significantly lower in astrocytomas (38%) and oligodendrogliomas (39%) compared to glioblastomas (55%) (Kruskal-Wallis: p=0.034*; Mann-Whitney: A vs G p=0.0172*; O vs G p=0.0348*).

These data further emphasize the specificity of IDHwt glioblastoma rRNA 2'Ome profiles compared to IDHmut HGGs and suggest that IDHwt glioblastomas display strong alterations of rRNA 2'Ome levels at some specific sites.

Glioblastomas display the most frequent site-specific rRNA 2'Ome alterations

To identify rRNA sites whose 2'Ome levels significantly differed between HGG histomolecular types and non-neoplastic tissues, we performed a systematic analysis of each of the 106 rRNA 2'Ome sites using the test cohort and applied two consecutive thresholds, a Kruskal-Wallis test with adjusted p-values < 0.05 and a cut-off value for mean $\Delta C\text{-scores}_{\text{max-min}} > 0.05$. From this screen, only 16 rRNA 2'Ome sites displayed a significant variation in their level of methylation in at least one HGG or non-neoplastic tissue (Fig.3). Pairwise comparisons for these 16 sites revealed that 4 and 6 sites displayed significant alterations in 2'Ome levels in high-grade astrocytomas and high-grade oligodendrogliomas, respectively, compared to non-neoplastic tissues (Fig.3B). In addition, rRNA 2'Ome levels appeared to be significantly increased on 6 sites in high-grade astrocytomas compared to high-grade oligodendrogliomas. Similar alterations in rRNA 2'Ome levels between IDHwt and IDHmut tumours were observed using the validation cohort (Fig.S5A). Finally, the main differences could be attributed to glioblastomas that displayed 12 and 14 of the 16 rRNA sites significantly altered compared to non-neoplastic samples or high-grade astrocytoma and oligodendrogliomas, respectively. Strikingly, rRNA 2'Ome levels were mostly lower in glioblastomas compared to non-neoplastic tissues, high-grade astrocytoma or high-grade oligodendrogliomas (Fig.3A). The same overall decrease in rRNA 2'Ome levels was confirmed in glioblastoma compared to non-neoplastic tissues using the technical cohort (Fig.S5B). Altogether, these results indicate that 2'Ome levels are altered at specific rRNA sites in HGGs, while glioblastomas display the highest frequency of alterations in rRNA 2'Ome levels compared to non-neoplastic cerebral cortex and other HGG histomolecular types.

Changes in C/D box snoRNA expression levels only partially explain alterations of rRNA 2'Ome levels

To investigate the origin of alterations of rRNA 2'Ome in HGGs, we focused on the expression of C/D snoRNAs (snoRDs), which guide in a sequence-specific manner the methyl-transferase FBL toward the rRNA nucleotide to methylate. We thus examined the correlation between levels of rRNA 2'Ome and related snoRDs. It was reported that snoRNA expression levels can be inferred from RiboMethSeq data^{37,38}. Thus, we used RiboMethSeq raw data from the NovaSeq platform and applied an in-house pipeline to overcome limitations of snoRNA analysis by next-generation sequencing (see Supplementary methods)^{39,40}. A strong and significant correlation (about 92%) between snoRNA levels either determined from RiboMethSeq or measured by RT-qPCR was observed in 9 glioma samples for 11 out of 12 selected snoRDs, thus validating our approach (Fig.S6A). Given that 2'Ome at a single rRNA site is catalyzed either by one or several snoRD^{15,41}, we restricted our analysis to the rRNA 2'Ome sites (n=46) guided by a single snoRD. No significant correlation was observed between levels of rRNA 2'Ome and of corresponding snoRDs among 37 sites (Fig.S6B). In contrast, a significant albeit relatively low positive correlation was observed for 9 pairs of snoRD/rRNA sites, the best correlation being that of the 18S-Am576 site and its associated SNORD93 ($\text{padj}=9.10^{-6}$, $r=0.68$) (Fig.S6B-C). Thus, alterations of rRNA 2'Ome levels cannot be exclusively attributed to changes in C/D box snoRNA expression levels.

The expression profile of ribosome biogenesis factors discriminates IDHmut and IDHwt HGGs

Since variations in snoRD expression levels cannot explain most of the changes observed in rRNA 2'Ome levels, we tested a novel hypothesis. Indeed, in cancer, variations of 2'Ome levels in rRNAs are believed to passively arise from the link between ribosome biogenesis (RiBi) and concomitant rRNA chemical modifications, whereby changes in ribosome synthesis impact the rate-limiting rRNA 2'Ome process and therefore influence 2'Ome profiles^{15,25,27}. Therefore, an overall decrease in rRNA 2'Ome levels observed in different cancer tissues may be caused by RiBi hyperactivation to sustain a high demand in protein synthesis necessary to support the highly proliferative cancer cells. As IDHwt glioblastomas possess a higher proliferative rate than IDHmut astrocytoma and oligodendrogliomas, including in our test cohort (based on

the mitotic index) (Fig.S4C-D), we hypothesized that the decrease in rRNA 2'Ome levels at specific positions in IDHwt glioblastomas could be due to a rate-limiting 2'Ome process caused by an exacerbated RiBi.

To investigate RiBi dysregulations across HGGs, we initially applied a gold-standard approach by analyzing levels of the 47S rRNA precursor (pre-rRNA), using Northern blot (Fig.S7A). However, this approach using tumor samples was challenging, notably due to the need for a large quantity of biological materials. Nevertheless, in a panel of 9 analyzable samples, IDHmut astrocytoma and oligodendrogliomas surprisingly seemed to express more pre-47S rRNAs than IDHwt glioblastomas. However, only two IDHwt glioblastoma samples were analyzed, therefore preventing us to draw any conclusion. To bypass this technical issue, we then measured the expression of a set of 20 genes involved in the early RiBi stages (referred to as "RiBi-gene set"). To reflect as much as possible this multistep process involving more than 200 factors⁷, we selected the RiBi-gene set implicated in the main RiBi process, including rRNA transcription (*NCL*, *NPM*, *POLR1A*, *TAF1A*, *TAF1B*, *TAF1C* and *UBTF*), rRNA maturation (*BOP1*, *PES1* and *WDR12*), snoRNA biogenesis (*RUVBL1*, *PIDH1D1* and *RUVBL2*), and H/ACA (*DKC1*, *GAR1*, *NHP2* and *NOP10*) and C/D box (*NOP56*, *SNU13* and *FBL*) snoRNP complexes (Fig.4A). Of note, three genes (*PIH1D1*, *RUVBL2* and *FBL*) are located on the long arm of chromosome 19 (19q), which undergoes a heterozygous deletion in high-grade oligodendrogliomas. A readout for RiBi at steady-state was determined by quantifying mRNA expression levels of these selected genes by medium throughput RT-qPCR in our validation series. mRNA levels were normalized against the median mRNA expression of 5 housekeeping genes, which did not significantly vary among the four groups (Fig.S7B).

To examine the association between expression levels of RiBi factors and HGGs, we first performed an unsupervised approach using a PCA based on the RiBi-gene set profile (Fig.4B). Interestingly, three main clusters were observed. A first large cluster, composed of both non-neoplastic tissues and IDHwt glioblastomas (NT/G cluster), was distinct from two other clusters corresponding to IDHmut oligodendrogliomas (O) and astrocytoma (A). PC1 (variance: 67.8%), in particular, separated the NT/G cluster from A/O clusters, while the PC2 (variance: 9%) distinguished the O cluster from others. These data suggest that the expression profile of only 20 RiBi factors discriminate HGGs.

To ensure consistency between the results of our classification and the expected outcome of the patients, we first calculated Pearson's correlation coefficients between the first 5 PC dimensions and OS or PFS as an internal control (Fig.4C and Fig.S7C). Consistently, we observed a significant association exclusively for PC1 and PC2, indicating that the clustering based on RiBi-gene set profiles provided by these two axes is sufficient to recapitulate all clinical data of interest. OS and PFS were significantly correlated with both PC1 and PC2 in a negative manner, indicating that samples clustering at the right-hand side of the PC1 and top of PC2, *i.e.*, IDHwt glioblastomas, display lower OS and PFS. Indeed, IDHwt glioblastoma patients exhibit the poorest OS (less than 30 months) and PFS (under 30 months), followed by IDHmut astrocytoma and oligodendroglioma patients that tend to cluster at the left part of PC1 and the top or bottom part of PC2, respectively.

Strikingly, we also identified a strong correlation between PC1 and PC2 axes, and the *IDH1/2* mutational and 1p/19q co-deletion status, respectively (Fig.S7D-E). Indeed, PC1 (G vs. A/O clusters) was significantly correlated with the *IDH1/2* mutational status while PC2 (A/G vs. O clusters) segregated HGG tumors based on the 1p/19q co-deletion status. Thus, expression profiling of the RiBi-gene set was strongly correlated with both clinical features and distinct genomic alterations of the HGG test cohort. Altogether, these results suggest that the expression signature of only 20 genes involved in ribosome biogenesis is sufficient to discriminate IDHwt from IDHmut HGG histomolecular types and that RiBi displays IDH mutational status-dependent alterations.

Ribosome biogenesis factors are highly expressed in IDHmut adult-type diffuse gliomas

Next, we individually compared mRNA expression levels of the 20 RiBi factors among the different HGGs (Fig.5 and Fig.S8A). Significant differences were observed in the expression of all tested RiBi factors between different groups (Mann Whitney test, Fig.S8A). Surprisingly, only a few RiBi genes were significantly differentially expressed in IDHwt glioblastomas compared to non-neoplastic samples (9 out of 20), with very moderate changes (≤ 2 -fold change). In contrast, IDHmut astrocytoma and oligodendrogliomas significantly overexpressed most of these RiBi genes (19 and 16 out of 20 RiBi genes, respectively). For instance, expression of *NCL*, which encodes a key factor in rRNA synthesis, increased by 2- and 3-fold in IDHmut astrocytoma and oligodendrogliomas, respectively ($p < 0.001$), while *NCL* expression levels in IDHwt samples

only slightly increased (Fig.5A and Fig.S8A). Likewise, the use of a second distinct set of primers to analyze *NCL* expression provided the exact same trend (Fig.S8B), therefore ruling out a potential technical caveat. These results suggest that ribosome biogenesis could be enhanced in IDHmut astrocytoma and oligodendrogliomas compared to IDHwt glioblastomas and non-neoplastic tissues.

Interestingly, genes located on chromosome 19q (*FBL*, *PIH1D1*, *RUVBL2*) displayed a particular expression pattern (Fig.5C, 5E and Fig.S7E). Like other genes involved in RiBi, *FBL*, *PIH1D1* and *RUVBL2* were significantly overexpressed in IDHmut astrocytomas compared to both IDHwt glioblastomas and non-neoplastic samples. However, mRNA expression levels in IDHmut oligodendrogliomas were lower than in IDHmut astrocytomas and displayed expression profiles resembling those of IDHwt glioblastomas. Thus, *FBL* was highly expressed exclusively in IDHmut astrocytomas, whereas its expression levels were equivalent in IDHmut oligodendrogliomas and IDHwt glioblastomas, as confirmed by a second set of primers (Fig.S8B). Considering that IDHmut oligodendroglioma samples exhibited a heterozygous deletion of *FBL*, *PIH1D1* and *RUVBL2* genes located on 1p/19q chromosomes, these data indicate that the specific expression profile observed for these genes in IDHmut oligodendrogliomas is likely due to a haploinsufficiency caused by genetic alterations. Interestingly, removal of these three genes in the RiBi-genes set still allowed us to distinguish IDHwt from IDHmut HGGs (data not shown), suggesting that copy number variation (CNVs) affecting RiBi gene expression does not impact the distinction between IDHwt and IDHmut, as expected. Therefore, the ribosome biogenesis pathway is strongly enhanced in IDHmut gliomas, *i.e.*, high-grade astrocytoma and oligodendroglioma, but remains moderately affected in IDHwt glioblastoma.

HGGs display distinct cytotoxicity to RNA pol I inhibitors CX5461 and BMH-21

Having identified an IDH mutational status-dependent alteration of RiBi in HGGs, we hypothesized that IDHmut and IDHwt HGGs display distinct cytotoxicity to RNA Pol I inhibitors, BMH-21 and CX5461, which inhibit the transcription of the 47S pre-rRNA and are promising new cancer treatments. We used a panel of 5 representative HGG cell lines, comprising IDHmut astrocytoma and IDHmut and 1p/19q codeleted oligodendroglioma cell lines (LGG85 and BT138/237, respectively) and IDHwt glioblastoma cell lines (5706 and N131520). Analyses of HGG spheroids in response to 72-

hour treatments with RNA pol I inhibitors showed that all spheroids were similarly sensitive to BMH-21 with an IC_{50} ranging from 1.06 to 1.56 μ M (Fig.6A-C), as recently observed⁴². However, CX5461 strongly impacted the viability of IDHmut astrocytoma and oligodendroglioma spheroids (IC_{50} ranging from 5.92 to 7.55 μ M), but not of IDHwt glioblastoma spheroids (Fig.6D-F). Hence, these results are consistent with our previous findings that IDHmut astrocytomas and oligodendrogliomas may be addicted to an enhanced RiBi pathway, therefore potentially sensitizing these AGD histomolecular types to clinically available RiBi inhibitors. Altogether, our results highlight the potency of RNA Pol I inhibitor usage as potential HGG therapy and further support an over-activation of the RiBi pathway in IDHmut astrocytomas and oligodendrogliomas compared to IDHwt glioblastomas and non-neoplastic tissues.

Discussion

High-grade adult-type diffuse gliomas (HGGs) are heterogeneous tumors associated with distinct, albeit poor, survival rates due to the lack of effective targeted therapies, in particular for the most aggressive histomolecular type, the IDHwt glioblastoma. Here, by performing the first concomitant analysis of rRNA 2'Ome and ribosome biogenesis in primary tumors, we report distinct, uncoupled alterations of rRNA epitran-scriptomics and ribosome biogenesis in IDHmut and IDHwt HGGs, therefore revealing specific dysregulations of the ribosome biology that constitute new IDH mutational status-associated hallmarks of HGGs.

In the last 7 years, alterations of rRNA 2'Ome profiles have been reported using a newly developed approach RiboMethSeq in numerous cellular models and only in three types of cancers, namely breast cancer, acute myeloid leukemia and diffuse large-B cell lymphoma (DLBCL)^{15,25,27,28}. Such alterations have been shown to be restricted to only 40% of the known rRNA 2'Ome sites, suggesting that only one third of the sites may possess regulatory functions on ribosome activity. We now show that rRNA 2'Ome profiles also vary in HGGs. As previously observed in other cancers, only a small subset of known rRNA 2'Ome sites display variability in their 2'Ome levels in HGGs, suggesting these positions can tolerate absence of 2'Ome. The 19 most variable rRNA 2'Ome sites were randomly distributed on the ribosome structure, suggesting no coordinated effects on functional domains of the ribosome. Notably, similar increases in rRNA 2'Ome levels at 18S_Am576 and decreases at 18S_Gm1447 were

observed in the most aggressive HGG type, glioblastoma, and breast cancer subtypes (triple negative or TNBC), suggesting a link between these sites and cancer aggressiveness²⁵. A recent study demonstrated that alterations of 2'Ome levels at a single rRNA site are sufficient to affect cell proliferation, a hallmark of cancer aggressiveness²⁶. Moreover, rRNA 2'Ome at 18S_Gm1447 was recently shown to support leukemic stem cell functions by modulating translation²⁸. Hence, whether these rRNA 2'Ome sites common to both HGGs and breast cancer contribute to the acquisition of cancer cell characteristics remains to be deciphered and could potentially represent new targetable vulnerabilities.

In IDHwt glioblastomas, alterations in rRNA 2'Ome levels mostly correspond to a decrease as observed in both the test and validation cohorts. In DLBCL, the global decrease in rRNA 2'Ome levels was correlated with the Ki67-estimated high proliferative rate of tumors. One hypothesis was that low rRNA 2'Ome levels indirectly resulted from an increase in rRNA synthesis associated with the hyperproliferative rate of cancer cells, which rendered components of the rRNA 2'Ome machinery limiting, although rRNA synthesis was not analyzed²⁷. Consistently, we observed specific alterations of rRNA 2'Ome in IDHwt glioblastomas, which are the most proliferative tumors and display the highest mitotic index in our test cohort. However, we surprisingly observed an elevated ribosome biogenesis in IDHmut astrocytomas and oligodendrogliomas compared to glioblastomas, suggesting that RiBi levels are not correlated with the proliferative rate, at least in HGGs, and cannot solely explain alterations of rRNA epitranscriptomics in HGGs. Even though the rate of ribosome biogenesis may contribute to regulating rRNA 2'Ome through a passive effect, additional molecular mechanisms should be further explored to identify the origin of rRNA 2'Ome alterations in cancer and understand the observed rRNA site- and cancer type-specificity. The mechanisms may include alterations of expressions and/or activities of RNA-binding proteins, such as DDX21 and FMRP, which contribute to the formation of *bona fide* functional snoRNP complexes^{29,43}. Here, we report that alterations of C/D box snoRNA expression could be sufficient to explain alterations of rRNA 2'Ome levels at some, but not all, rRNA sites. The evolution of annotation and/or knowledge in biology of C/D box snoRNAs may fill the gap to better understand causes of rRNA 2'Ome alterations in cancer. Altogether, our findings that main HGG histomolecular types are associated with alterations in either ribosome quantity or quality, challenge the hypothesis that the decrease

in rRNA 2'Ome levels mainly results from a passive effect caused by an exacerbated ribosome biogenesis.

Our data reveal that IDHmut HGGs, including both high-grade astrocytoma and oligodendroglioma, display the highest expression of ribosome biogenesis factors, suggesting an increase in ribosome biogenesis. Whether dysregulations of *IDH1/2* functions, notably through the production of the oncometabolite D-2-hydroxyglutarate, could directly impact the regulation of ribosome biogenesis would need to be further explored. Nevertheless, the specificity of ribosome biogenesis alterations in HGGs offers novel perspectives for clinical applications. Building on our observations, we found that HGGs are sensitive to the newly developed RNA pol I inhibitors, CX5461 and BMH-21, the former being successfully evaluated in clinical trials in advanced solid and hematological cancers⁷. Sensitivity of HGGs to RNA pol I inhibitors CX5461 and BMH-21 has already been reported^{42,44,45}, even though discrepancies regarding the sensitivity of glioblastomas to CX5461 exist between our data and previous ones, possibly due to differences in experimental settings and genetic backgrounds of tested cell lines. In particular, the 3D culture conditions could decrease drug sensitivity compared to 2D culture conditions, as already reported⁴⁶. In addition, the differential sensitivity of glioblastomas to CX5461 and BMH-21 could be attributed to off-target effects of these molecules as these RNA Pol I inhibitors act through distinct mechanisms and are known to affect several cellular pathways, including DNA repair^{10,34,47}. Thus, whether the activity of these compounds may also rely on the genetic background of tested models impacting the different sensitivities of HGG types to CX5461 and BMH-21, should be further investigated.

Altogether, our data indicate that alterations of the ribosome biology in HGGs are dependent on the IDH mutational status and could represent targetable features in clinic. Thus, recent discoveries in the field of ribosomes have opened new avenues not only for a better understanding of cellular processes that contribute to HGG development and aggressiveness but also for designing future HGG type-specific therapeutic strategies.

Conflict of interest

The authors have no conflicts of interest to declare.

Ethical Approval

All the experiment protocol for involving human was in accordance with the guidelines of French regulation. Written informed consent was obtained from all patients.

Fundings

This work was supported by INCa (PLBio 2019-138 MARACAS), the French Association pour la Recherche sur les Tumeurs Cérébrales (ARTC), the Cancéropôle Lyon Auvergne Rhône-Alpes (AAP international 2021 MARACAS.v3.0), the Ligue Contre le Cancer Auvergne-Rhône-Alpes and the SIRIC program (INCa-DGOS-Inserm_12563, LyRICAN). HP and NEHM were recipients of PhD fellowships from Ligue Nationale Contre le Cancer. JH was recipient of PhD fellowship from French Minister of Research.

Author contribution

HP, NEHM, SB, JH, FB, VA, MC, JP, DB, LCV, SD performed and analysed experiments. HP, NEHM, JK, ET, DB performed statistical descriptions and bioinformatic analyses. HP, TC, AF, JK, ET, LT, AV developed bioinformatic tools. LCV, EH, MS provided cell lines. DM, FD provided human samples and clinical data. AF, JK, ET, VA, SG, MSS, EH, MS, DM, FC, VM, SB supervised experimental process. HP, NEHM, SB, JK, SG, FD, VM and SD interpreted the data. VM and SD shaped the clinical and research question and supervised the project coordination. AV, MSS, EH, MS, MG, JJD, FD, VM and SD provided financial supports. HP, NEHM, VM and SD wrote the first draft of the manuscript. All authors have read and approved the manuscript.

Availability of datasets

The generated RiboMethSeq data are available in the GEO profile (GSE224104, token for reviewer access: qhabqswmfzotlwh). The datasets include the fastq of each sample, a C-score matrix for each cohort after batch effect adjustment using ComBat-seq and a matrix summarizing the clinical data.

Acknowledgements

We would like to thank all the people involved in this study, including the patients and their families. We thank Drs A Idbaih (ICM, Paris, France), JP Hugnot (IGF, Montpellier, France) and K Ligon (Brigham and Women's Hospital, Boston, USA) for generously providing cell lines. We thank platform staffs that have not been referred as co-authors: NeuroBioTec (CRB HCL, Lyon, France, Biobank BB-0033-00046); Organoid platform (CRCL, Lyon, France); Gilles Thomas Bioinformatic platform (CRCL, Lyon, France); Cancer Genomic platform (CRCL, Lyon, France). **The manuscript has been edited by Brigitte Manship (CRCL, Lyon, France).**

References

1. Wen PY, Weller M, Lee EQ, et al. Glioblastoma in adults: a Society for Neuro-Oncology (SNO) and European Society of Neuro-Oncology (EANO) consensus review on current management and future directions. *Neuro Oncol.* 2020;22(8):1073-1113. doi:10.1093/NEUONC/NOAA106
2. Lapointe S, Perry A, Butowski NA. Primary brain tumours in adults. *Lancet.* 2018;392(10145):432-446. doi:10.1016/S0140-6736(18)30990-5
3. Lassman AB, Hoang-Xuan K, Polley MYC, et al. Joint Final Report of EORTC 26951 and RTOG 9402: Phase III Trials With Procarbazine, Lomustine, and Vincristine Chemotherapy for Anaplastic Oligodendroglial Tumors. *J Clin Oncol.* 2022;40(23):2539-2545. doi:10.1200/JCO.21.02543
4. van den Bent MJ, Tesileanu CMS, Wick W, et al. Adjuvant and concurrent temozolomide for 1p/19q non-co-deleted anaplastic glioma (CATNON; EORTC study 26053-22054): second interim analysis of a randomised, open-label, phase 3 study. *Lancet Oncol.* 2021;22(6):813-823. doi:10.1016/S1470-2045(21)00090-5
5. Bastide A, David A. The ribosome, (slow) beating heart of cancer (stem) cell. *Oncogenesis* 2018 7:4. 2018;7(4):1-13. doi:10.1038/s41389-018-0044-8
6. Barna M, Pusic A, Zollo O, et al. Suppression of Myc oncogenic activity by ribosomal protein haploinsufficiency. *Nature* 2008 456:7224. 2008;456(7224):971-975. doi:10.1038/nature07449
7. Catez F, Dalla Venezia N, Marcel V, Zorbas C, Lafontaine DLJ, Diaz JJ. Ribosome biogenesis: An emerging druggable pathway for cancer therapeutics. *Biochem Pharmacol.* 2019;159:74-81. doi:10.1016/J.BCP.2018.11.014
8. Penzo M, Montanaro L, Treré D, Derenzini M. The Ribosome Biogenesis—Cancer Connection. *Cells* 2019, Vol 8, Page 55. 2019;8(1):55. doi:10.3390/CELLS8010055
9. Bywater MJ, Poortinga G, Sanij E, et al. Inhibition of RNA Polymerase I as a Therapeutic Strategy to Promote Cancer-Specific Activation of p53. *Cancer Cell.* 2012;22(1):51-65. doi:10.1016/J.CCR.2012.05.019
10. Peltonen K, Colis L, Liu H, et al. A targeting modality for destruction of RNA polymerase I that possesses anticancer activity. *Cancer Cell.* 2014;25(1):77-90. doi:10.1016/J.CCR.2013.12.009
11. Hilton J, Gelmon K, Bedard PL, et al. Results of the phase I CCTG IND.231 trial of CX-5461 in patients with advanced solid tumors enriched for DNA-repair deficiencies.

- 653 *Nature Communications* 2022 13:1. 2022;13(1):1-12. doi:10.1038/s41467-022-31199-
654 2
- 655 12. Khot A, Brajanovski N, Cameron DP, et al. First-in-human RNA polymerase I tran-
656 scription inhibitor CX-5461 in patients with advanced hematologic cancers: Results of
657 a phase I dose-escalation study. *Cancer Discov.* 2019;9(8):1036-1049.
658 doi:10.1158/2159-8290.CD-18-1455/333397/AM/FIRST-IN-HUMAN-RNA-POLY-
659 MERASE-I-TRANSCRIPTION
- 660 13. Xu H, Di Antonio M, McKinney S, et al. CX-5461 is a DNA G-quadruplex stabilizer
661 with selective lethality in BRCA1/2 deficient tumours. *Nature Communications* 2017
662 8:1. 2017;8(1):1-18. doi:10.1038/ncomms14432
- 663 14. Marcel V, Catez F, Diaz JJ. Ribosome heterogeneity in tumorigenesis: the rRNA point
664 of view. *Mol Cell Oncol.* 2015;2(3). doi:10.4161/23723556.2014.983755
- 665 15. Jaafar M, Paraqindes H, Gabut M, Diaz JJ, Marcel V, Durand S. 2'O-Ribose Methyla-
666 tion of Ribosomal RNAs: Natural Diversity in Living Organisms, Biological Processes,
667 and Diseases. *Cells* 2021, Vol 10, Page 1948. 2021;10(8):1948.
668 doi:10.3390/CELLS10081948
- 669 16. Miller SC, MacDonald CC, Kellogg MK, Karamysheva ZN, Karamyshev AL. Special-
670 ized Ribosomes in Health and Disease. *International Journal of Molecular Sciences*
671 2023, Vol 24, Page 6334. 2023;24(7):6334. doi:10.3390/IJMS24076334
- 672 17. Xue S, Barna M. Specialized ribosomes: a new frontier in gene regulation and organis-
673 mal biology. *Nature Reviews Molecular Cell Biology* 2012 13:6. 2012;13(6):355-369.
674 doi:10.1038/nrm3359
- 675 18. Genuth NR, Barna M. Heterogeneity and specialized functions of translation machin-
676 ery: from genes to organisms. *Nature Reviews Genetics* 2018 19:7. 2018;19(7):431-
677 452. doi:10.1038/s41576-018-0008-z
- 678 19. Larionova TD, Bastola S, Aksinina TE, et al. Alternative RNA splicing modulates ribo-
679 somal composition and determines the spatial phenotype of glioblastoma cells. *Nat Cell*
680 *Biol.* 2022;24(10):1541-1557. doi:10.1038/S41556-022-00994-W
- 681 20. Gabut M, Bourdelais F, Cells SD, 2020 undefined. Ribosome and translational control
682 in stem cells. *mdpi.com.* 2020;9(2). doi:10.3390/cells9020497
- 683 21. Shirakawa Y, Hide T, Yamaoka M, et al. Ribosomal protein S6 promotes stem-like
684 characters in glioma cells. *Cancer Sci.* 2020;111(6):2041-2051.
685 doi:10.1111/CAS.14399
- 686 22. Hide T, Shibahara I, Inukai M, Shigeeda R, Kumabe T. Ribosomes and Ribosomal Pro-
687 teins Promote Plasticity and Stemness Induction in Glioma Cells via Reprogramming.
688 *Cells* 2022, Vol 11, Page 2142. 2022;11(14):2142. doi:10.3390/CELLS11142142
- 689 23. Erales J, Marchand V, Panthu B, et al. Evidence for rRNA 2'-O-methylation plasticity:
690 Control of intrinsic translational capabilities of human ribosomes. *Proc Natl Acad Sci*
691 *U S A.* 2017;114(49):12934-12939.
692 doi:10.1073/PNAS.1707674114/SUPPL_FILE/PNAS.1707674114.SD03.XLSX
- 693 24. Marcel V, Ghayad SE, Belin S, et al. P53 Acts as a Safeguard of Translational Control
694 by Regulating Fibrillarin and rRNA Methylation in Cancer. *Cancer Cell.*
695 2013;24(3):318-330. doi:10.1016/J.CCR.2013.08.013
- 696 25. Marcel V, Kielbassa J, Marchand V, et al. Ribosomal RNA 2'O-methylation as a novel
697 layer of inter-tumour heterogeneity in breast cancer. *NAR Cancer.* 2020;2(4).
698 doi:10.1093/NARCAN/ZCAA036
- 699 26. Jansson MD, Häfner SJ, Altinel K, et al. Regulation of translation by site-specific ribo-
700 somal RNA methylation. *Nature Structural & Molecular Biology* 2021 28:11.
701 2021;28(11):889-899. doi:10.1038/s41594-021-00669-4

27. Krogh N, Asmar F, Côme C, Munch-Petersen HF, Grønbaek K, Nielsen H. Profiling of ribose methylations in ribosomal RNA from diffuse large B-cell lymphoma patients for evaluation of ribosomes as drug targets. *NAR Cancer*. 2020;2(4). doi:10.1093/NAR-CAN/ZCAA035
28. Zhou F, Aroua N, Liu Y, et al. A Dynamic rRNA Ribomethylome Drives Stemness in Acute Myeloid Leukemia. *Cancer Discov*. 2022;13:OF1-OF17. doi:10.1158/2159-8290.CD-22-0210
29. Zhou F, Liu Y, Rohde C, et al. AML1-ETO requires enhanced C/D box snoRNA/RNP formation to induce self-renewal and leukaemia. *Nat Cell Biol*. 2017;19(7):844-855. doi:10.1038/NCB3563
30. Nachmani D, Bothmer AH, Grisendi S, et al. Germline NPM1 mutations lead to altered rRNA 2'-O-methylation and cause dyskeratosis congenita. *Nat Genet*. 2019;51(10):1518-1529. doi:10.1038/S41588-019-0502-Z
31. Nguyen Van Long F, Lardy-Cleaud A, Carène D, et al. Low level of Fibrillarin, a ribosome biogenesis factor, is a new independent marker of poor outcome in breast cancer. *BMC Cancer*. 2022;22(1):1-12. doi:10.1186/S12885-022-09552-X/FIGURES/3
32. Marchand V, Ayadi L, el Hajj A, Blanloeil-Oillo F, Helm M, Motorin Y. High-Throughput Mapping of 2'-O-Me Residues in RNA Using Next-Generation Sequencing (Illumina RiboMethSeq Protocol). *Methods Mol Biol*. 2017;1562:171-187. doi:10.1007/978-1-4939-6807-7_12
33. Pichot F, Marchand V, Ayadi L, Bourguignon-Igel V, Helm M, Motorin Y. Holistic Optimization of Bioinformatic Analysis Pipeline for Detection and Quantification of 2'-O-Methylations in RNA by RiboMethSeq. *Front Genet*. 2020;11:38. doi:10.3389/FGENE.2020.00038/BIBTEX
34. Drygin D, Lin A, Bliesath J, et al. Targeting RNA polymerase I with an oral small molecule CX-5461 inhibits ribosomal RNA synthesis and solid tumor growth. *Cancer Res*. 2011;71(4):1418-1430. doi:10.1158/0008-5472.CAN-10-1728
35. Birkedal U, Christensen-Dalsgaard M, Krogh N, Sabarinathan R, Gorodkin J, Nielsen H. Profiling of ribose methylations in RNA by high-throughput sequencing. *Angew Chem Int Ed Engl*. 2015;54(2):451-455. doi:10.1002/ANIE.201408362
36. Zhang Y, Parmigiani G, Johnson WE. ComBat-seq: batch effect adjustment for RNA-seq count data. *NAR Genom Bioinform*. 2020;2(3). doi:10.1093/NARGAB/LQAA078
37. Sharma S, Marchand V, Motorin Y, Lafontaine DLJ. Identification of sites of 2'-O-methylation vulnerability in human ribosomal RNAs by systematic mapping. *Sci Rep*. 2017;7(1). doi:10.1038/S41598-017-09734-9
38. Delhermite J, Tafforeau L, Sharma S, et al. Systematic mapping of rRNA 2'-O methylation during frog development and involvement of the methyltransferase Fibrillarin in eye and craniofacial development in *Xenopus laevis*. *PLoS Genet*. 2022;18(1):e1010012. doi:10.1371/JOURNAL.PGEN.1010012
39. Deschamps-Francoeur G, Boivin V, Abou Elela S, Scott MS. CoCo: RNA-seq read assignment correction for nested genes and multimapped reads. *Bioinformatics*. 2019;35(23):5039-5047. doi:10.1093/BIOINFORMATICS/BTZ433
40. Bergeron D, Laforest C, Carpentier S, et al. SnoRNA copy regulation affects family size, genomic location and family abundance levels. *BMC Genomics*. 2021;22(1). doi:10.1186/S12864-021-07757-1
41. Bergeron D, Paraquindes H, Fafard-Couture É, et al. snoDB 2.0: an enhanced interactive database, specializing in human snoRNAs. *Nucleic Acids Res*. 2023;51(D1):D291-D296. doi:10.1093/NAR/GKAC835

- 750 42. Zisi A, Kanellis DC, Moussaud S, et al. Small Molecule-mediated Disruption of Ribo-
751 some Biogenesis Synergizes With FGFR Inhibitors to Suppress Glioma Cell Growth.
752 *Neuro Oncol*. Published online December 30, 2022. doi:10.1093/NEUONC/NOAC286
- 753 43. D'Souza MN, Gowda NKC, Tiwari V, et al. FMRP Interacts with C/D Box snoRNA in
754 the Nucleus and Regulates Ribosomal RNA Methylation. *iScience*. 2018;9:399-411.
755 doi:10.1016/J.ISCI.2018.11.007
- 756 44. Li G, Shen J, Cao J, et al. Alternative splicing of human telomerase reverse transcrip-
757 tase in gliomas and its modulation mediated by CX-5461. *Journal of Experimental and*
758 *Clinical Cancer Research*. 2018;37(1):1-13. doi:10.1186/S13046-018-0749-8/FIG-
759 URES/7
- 760 45. Chiu YC, Chen HIH, Zhang T, et al. Predicting drug response of tumors from inte-
761 grated genomic profiles by deep neural networks. *BMC Med Genomics*.
762 2019;12(1):143-155. doi:10.1186/S12920-018-0460-9/TABLES/5
- 763 46. El Hassouni B, Mantini G, Immordino B, Peters GJ, Giovannetti E. CX-5461 Inhibits
764 Pancreatic Ductal Adenocarcinoma Cell Growth, Migration and Induces DNA Dam-
765 age. *Molecules* 2019, Vol 24, Page 4445. 2019;24(24):4445. doi:10.3390/MOLE-
766 CULES24244445
- 767 47. Xu H, di Antonio M, McKinney S, et al. CX-5461 is a DNA G-quadruplex stabilizer
768 with selective lethality in BRCA1/2 deficient tumours. *Nature Communications* 2017
769 8:1. 2017;8(1):1-18. doi:10.1038/ncomms14432

Figure Legends

Figure 1. rRNA 2'Ome levels vary in high-grade adult-type diffuse gliomas. An unsupervised hierarchical clustering of C-scores at the 106 known rRNA 2'O-ribose methylated (2'Ome) sites was performed in a test cohort of 40 high-grade (3-4) adult-type diffuse glioma (HGG) samples and 6 non-tumoral, non-neoplastic cerebral cortex (NT) samples. C-scores are represented by a color scale from 0 (black) to 1 (yellow). IDHwt glioblastomas (G), high-grade astrocytomas (A), high-grade oligodendrogliomas (O) and non-neoplastic (NT) samples are depicted in pink, green, purple, and grey, respectively. The mean C-score for each site across the 46 samples is shown on the right-hand side of the graph. 86 sites have a mean C-score higher than 0.9 (black) and 20 sites lower than 0.9 (red).

Figure 2. The most variable rRNA 2'Ome sites are sufficient to distinguish different HGG types. (A) Distribution of the interquartile range (IQR) of the C-score to determine the C-score variability across HGG samples of the test cohort (n=40). rRNA 2'Ome sites are ranked by increasing IQR value. The IQR distribution curve is plotted at the right-hand side of the graph. The "most variable sites" correspond to those with an IQR higher than median + 2 × median absolute deviation (mad) and were colored in red (19 sites). **(B-D)** Unsupervised Principal Component Analysis (PCA) based on C-scores of the 19 most variable sites as identified in (A). **Independent PCA was performed on IDHwt glioblastoma (G, pink circle), high-grade astrocytoma (A, green triangle) and high-grade oligodendroglioma (O, purple diamond) samples of both test (B, n=40) and validation (n=23) cohorts. Validation cohort samples were projected on PCA of the test cohort (D).** Percentage of variance explained by PC1 and PC2 are indicated. 95 % confidence ellipsoids around the centroid of each group (larger pink circle, green triangle and purple diamond) are indicated.

Figure 3. rRNA 2'Ome levels are differently altered in HGG types. (A) **Box plots showing the distribution of C-score in HGG and non-neoplastic samples of the test cohort for 16 rRNA 2'O-ribose methylated (2'Ome) sites that exhibited both statistically and biologically significant alterations between groups. These sites were identified using both Kruskal-Wallis statistical tests (with an adjusted p-value threshold of < 0.05)**

and a mean $\Delta C\text{-score}_{\text{max-min}} > 0.05$ (absolute difference between the highest and lowest mean C-score). The adjusted p-values corresponding to the statistical tests are indicated on the bottom left-hand side of each panel and median C-scores are represented by a black line within the box plots. **(B)** Pairwise comparison of mean C-score groups for the 16 significantly deregulated rRNA 2'Ome sites in the test cohort. Positive (UP) and negative (DOWN) $\Delta C\text{-score}_{\text{group1-group2}}$ are shown in blue and red, respectively. Adjusted p-values: *: $p < 0.05$; **: $p < 0.01$; ***: $p < 0.001$; ****: $p < 0.0001$; ns, not significant.

Figure 4. Expression profiles of RiBi factors distinguish HGG types. **(A)** Panel of genes involved in ribosome biogenesis constituting the 20 RiBi-gene set analyzed in HGG and non-neoplastic samples. Genes located on the short arm of chromosome 1 (1p) or long arm of chromosome 19 (19q), which are heterozygously deleted in high-grade oligodendrogliomas, are indicated. **(B)** A principal component analysis (PCA) based on the mRNA expression profile of the RiBi-gene set. Each dot represents a non-neoplastic (NT, grey square), IDHwt glioblastoma (G, pink circle), high-grade astrocytoma (A, green triangle) or high-grade oligodendroglioma (O, purple diamond) sample. Ellipsoids shows 90% confidence interval around the centroid (larger grey square, pink circle, green triangle, and purple diamond) of each group. Percentage of variance explained by PC1 and PC2 are indicated. **(C)** A heatmap showing Pearson's correlation coefficients of PC1 to PC5 axes with the overall survival (OS), progression-free survival (PFS) and mitotic index. R-values are depicted by different colors from -0.6 (red, negative correlation) to 0.6 (blue, positive correlation). Significant correlations are indicated by an asterisk: ** $p < 0.01$; *** $p < 0.001$.

Figure 5. High-grade astrocytomas and oligodendrogliomas display the highest increased expression in ribosome biogenesis factors. Box plots showing relative mRNA expression levels determined by RT-qPCR analysis of the RiBi genes implicated in rRNA **(A)** transcription and **(B)** maturation, **(C)** snoRNA biogenesis or associated to **(D)** H/ACA box and **(E)** C/D box snoRNAs in IDHwt glioblastomas (G, pink), high-grade astrocytomas (A, green), high-grade oligodendrogliomas (O, purple) and non-neoplastic (NT, grey) samples. *FBL*, *PIH1D1* and *RUVBL2* are located on chromosomes 1p or 19q.

Figure 6. Glioma spheroids reveal distinct histomolecular type-dependent sensitivity to ribosome biogenesis inhibitors. **(A)** Representative high-content screening microscopy images of 5706, N131520, BT138, BT237 and LGG85 cell line spheroids treated or not (DMSO) with 10 μ M of BMH-21 for 72 h. Hoechst and CellTox labelling are depicted in blue and green, respectively. Cell lines representative of glioblastomas, high-grade oligodendrogliomas and astrocytomas are shown in pink, purple and green, respectively. **(B)** Representative graphs indicating the viability percentage in response to increasing BMH-21 concentrations in 5706, N131520, BT138, BT237 and LGG85 cell line spheroids. Cell lines representative of IDHwt glioblastomas, IDHmut oligodendrogliomas and astrocytomas are framed in pink, purple and green, respectively. **(C)** A table indicating means and standard deviations (SD) of BMH-21 IC₅₀ calculated from graphs displayed in (B) (n=7). (D), (E) and (F) as in (A) (B) and (C), respectively, for CX5461 (n=3).

IDHwt and IDHmut adult-type diffuse gliomas display distinct alterations in ribosome biogenesis and 2'O-methylation of ribosomal RNA

Hermes PARAQUINDES^{1,2,#}, Nour-EI-Houda MOURKSI^{1,#}, Samantha BALLESTA^{1,3,#}, Jordan HEDJAM¹, Fleur BOURDELAIS^{1,4}, Tanguy FENOUIL^{1,9}, Thiébaud PICART^{1,9}, Frédéric CATEZ¹, Théo COMBE^{1,2}, Anthony FERRARI^{1,2}, Janice KIELBASSA², Emilie THOMAS^{1,2}, Laurie TONON^{1,2}, Alain VIARI^{1,2,5}, Valéry ATTIGNON^{1,6}, Marjorie CARRE^{1,6}, Jessie PERROSSIER^{1,6}, Stéphane GIRAUD^{1,3}, Christophe VANBELLE^{1,12}, Mathieu GABUT¹, Danny BERGERON⁷, Michelle S SCOTT⁷, Luis CASTRO VEGA⁸, Nathalie MAGNE⁸, Emmanuelle HUILLARD⁸, Marc SANSON⁸, David MEYRONET^{1,9}, Jean-Jacques DIAZ¹, François DUCRAY^{1,11,*}, Virginie MARCEL^{1,#,*}, Sébastien DURAND^{1,#,*}

1. LabEx Dev2CAN, Institut Convergence Plascan, Centre de Recherche en Cancérologie de Lyon, Inserm U1052, CNRS UMR5286, Université de Lyon, Université Claude Bernard Lyon 1, Centre Léon Bérard, CEDEX 08, F-69373 Lyon, France

2. Synergie Lyon Cancer, Gilles Thomas Bioinformatics Platform, Centre Léon Bérard, CEDEX 08, F-69373 Lyon, France

3. Plateforme organoïdes 3D-ONCO, Université de Lyon, Université Claude Bernard Lyon 1, Inserm U1052, CNRS UMR5286, Centre Léon Bérard, Centre de Recherche en Cancérologie de Lyon (CRCL), Lyon, 69373, France

4. Inovarion, 75005, Paris, France.

5. INRIA Grenoble Rhône-Alpes, 38330 Montbonnot-Saint-Martin, France

6. Cancer Genomics Platform, Centre de Recherche en Cancérologie de Lyon, CEDEX 08, F-69373 Lyon, France

7. Département de biochimie et génomique fonctionnelle, Faculté de médecine et des sciences de la santé, Université de Sherbrooke, Sherbrooke, Québec J1E 4K8, Canada

8. Sorbonne Université, Inserm, CNRS, UMR51127, Institut du Cerveau, ICM, AP-HP, Hôpitaux Universitaires La Pitié Salpêtrière – Charles Foix, Service de Neurologie 2-Mazarin, 75013 Paris, France

9. Hospices Civils de Lyon, Laboratoire de biologie médicale et d'anatomie pathologique

10. Hospices Civils de Lyon, Service de Neurochirurgie tumorale et vasculaire, Hôpital
Pierre Wertheimer

11. Hospices Civils de Lyon, Service de neuro-oncologie, Hôpital Pierre Wertheimer

12. Plateforme d'Imagerie Cellulaire, Université de Lyon, Université Claude Bernard
Lyon 1, Inserm U1052, CNRS UMR5286, Centre Léon Bérard, Centre de Recherche
en Cancérologie de Lyon (CRCL), Lyon, 69373, France

Equal contribution as co-first or co-last authors

* Corresponding authors: francois.ducray@chu-lyon.fr, virginie.marcel@lyon.uni-
cancer.fr and sebastien.durand@inserm.fr

Keywords

glioma, IDH mutational status, ribosome, epitranscriptomics, ribosome biogenesis factors

Running title

Ribosome alterations in high-grade gliomas

Issue section

Basic and translational investigation

Key points (3)

- rRNA 2'Ome profiling distinguishes IDHwt and IDHmut adult-type diffuse gliomas
- Elevated expression of ribosome biogenesis factors is correlated with IDH mutational status
- High grade adult-type diffuse gliomas differentially respond to the RNA Pol I inhibitors BMH-21 and CX5461

Word count: 4991

Abstract

Background: High-grade adult-type diffuse gliomas (HGGs) constitute a heterogeneous group of aggressive tumors that are mostly incurable. Recent advances highlighting the contribution of ribosomes to cancer development have offered new clinical perspectives. Here, we uncovered that IDHwt and IDHmut HGGs display distinct alterations of ribosome biology, in terms of rRNA epitranscriptomics and ribosome biogenesis, which could constitute novel hallmarks that can be exploited for the management of these pathologies.

Methods: We analyzed (i) the ribosomal RNA 2'O-ribose methylation (rRNA 2'Ome) using RiboMethSeq and in-house developed bioinformatics tools (<https://github.com/RibosomeCRCL/ribomethseq-nf> and [rRMSAnalyzer](#)) on three independent cohorts compiling 71 HGGs (IDHwt n=30, IDHmut n=41) and 9 non-neoplastic samples, (ii) the expression of ribosome biogenesis factors using medium throughput RT-qPCR as a readout of ribosome biogenesis, and (iii) the sensitivity of 5 HGG cell lines to RNA Pol I inhibitors (CX5461, BMH21).

Results: Unsupervised analysis demonstrated that HGGs could be distinguished based on their rRNA 2'Ome epitranscriptomic profile, with IDHwt glioblastomas displaying the most significant alterations of rRNA 2'Ome at specific sites. In contrast, IDHmut HGGs are largely characterized by an overexpression of ribosome biogenesis factors compared to non-neoplastic tissues or IDHwt glioblastomas. Finally, IDHmut HGG-derived spheroids display higher cytotoxicity to CX5461 than IDHwt glioblastoma, while all HGG spheroids display a similar cytotoxicity to BMH-21.

Conclusion: In HGGs, IDH mutational status is associated with specific alterations of the ribosome biology and with distinct sensitivities to RNA Pol I inhibitors.

Importance of the study (146 words)

Consistent multi-omics studies have shown that high-grade adult-type diffuse gliomas (HGGs) can be classified into three main groups, *i.e.*, IDHmut and 1p/19q codeleted oligodendrogliomas, IDHmut astrocytomas and IDHwt glioblastomas, based on their genetic, transcriptomic and DNA methylation profiles. Recent advances have highlighted the contribution of ribosomes to cancer development and have offered new clinical perspectives. Herein, we show that ribosomal RNA (rRNA) epitranscriptomic and ribosome biogenesis are different in distinct HGG types. We uncovered that IDHwt glioblastomas display the most prominent defects in rRNA epitranscriptomics, whereas IDHmut astrocytomas and oligodendrogliomas exhibit enhanced expression of ribosome biogenesis factors compared to IDHwt glioblastomas. Moreover, based on their IDH mutational status, HGG-derived cell lines displayed distinct responses to CX5461 and BMH-21, two clinically-evaluated inhibitors of the RNA Pol I that transcribes rDNAs. This study identifies a connection between HGG oncogenesis and the ribosome biology, and highlights new therapeutic strategies.

111 Introduction

112 High-grade adult-type diffuse gliomas (HGGs) are brain tumors resembling glial cells
 113 that display highly heterogeneous prognoses and treatment responses. HGGs com-
 114 prise three main histomolecular types, astrocytomas, oligodendrogliomas and glioblas-
 115 tomas, based notably on the mutational status of *isocitrate dehydrogenase (IDH)* 1 and
 116 2^{1,2}. Indeed, glioblastomas are IDHwt, whereas astrocytomas and oligodendrogliomas
 117 are IDHmut, and can be further discriminated by the heterozygous 1p19q co-deletion
 118 occurring in oligodendrogliomas. IDHwt and IDHmut HGGs are associated with distinct
 119 epigenetic and transcriptomic dysregulations, leading to cancer-specific features.
 120 Thus, despite important advances in their histomolecular classification and under-
 121 standing of their oncogenesis, HGGs remain mostly incurable. For instance, grade 4
 122 IDHwt glioblastoma patients treated with the conventional combination of surgery, ra-
 123 diotherapy and temozolomide (TMZ) chemotherapy, display a median survival of only
 124 15 months. Grade 3 IDHmut astrocytoma and oligodendroglioma patients treated with
 125 radiotherapy and chemotherapy exhibit a much better outcome with a median survival
 126 of 10 and 15 years, respectively, nevertheless 20 to 30% of the patients die within the
 127 first five years after diagnosis^{3,4}. Therefore, the identification of novel molecular mech-
 128 anisms dysregulated in distinct HGG histomolecular types may significantly improve
 129 current therapeutic options.

130 Several studies highlighted that ribosome biogenesis (RiBi) and functions are altered
 131 in cancer cells and that ribosomes can support oncogenic functions⁵. For instance, the
 132 c-MYC oncogenic activity is in part supported by a dysregulation of genes implicated
 133 in RiBi and global protein synthesis⁶. In addition, levels of RiBi are generally increased
 134 in cancer cells to support the high protein synthesis demand caused by their exacer-
 135 bated proliferation rate^{7,8} and therefore, the inhibition of rRNA synthesis specifically
 136 kills cancer cells without affecting normal cells^{9,10}. Such observations led to the devel-
 137 opment of molecules specifically inhibiting RiBi that showed objective responses in
 138 clinical trials, such as CX5461^{11–13}.

139 In addition to alteration of RiBi, recent observations suggest that variations of ribosome
 140 composition could also occur in cancer and be involved in disease etiology^{14–16}. The
 141 ribosome is composed of 80 ribosomal proteins and 4 ribosomal RNAs (rRNAs), the
 142 latter supporting the enzymatic activity of the peptidyl-bond formation during the trans-
 143 lation of mRNAs into proteins. For many decades, the ribosome was considered as a
 144 monolithic entity displaying a similar composition in all cells constituting an organism.

However, it appears now that the ribosome composition can display some degree of variations, both at the level of ribosomal proteins and rRNA chemical modifications, which contributes to modulate intrinsic translational activities that could shape particular phenotypes^{17,18}. Variations of the ribosome composition at ribosomal protein levels have been reported in HGGs^{19–22}. In IDHwt glioblastomas, the overexpression of the ribosomal protein RPS6 was shown to promote acquisition of glioma stem cell properties, a hallmark of the most aggressive IDHwt glioblastomas^{20–22}. In addition, RPL22L1 isoforms are expressed in distinct regions of IDHwt glioblastomas through alternative splicing and induce the production of ribosomes with specific compositions, which promote translational bias towards specific mRNA subsets^{15,19,23–30}. In addition to ribosomal proteins, the chemical modifications of rRNA represent one of the major contributors to ribosome heterogeneity and led to the emergence of the notion of rRNA epitranscriptomics¹⁵. One of the main modifications, the methylation of the rRNA 2'O-ribose (rRNA 2'Ome), occurs at 106 known rRNA sites in humans and the 2'Ome at specific positions are essential for rRNA activity. The catalysis of rRNA 2'Ome is performed by an rRNA methylation complex composed of the methyl-transferase fibrillarin (FBL) and a single non-coding C/D box small nucleolar RNA (snoRNA or snoRD), which guides FBL at specific sites by base-pairing¹⁵. Hence, modulations of *FBL* or snoRD expression are sufficient to affect rRNA 2'Ome^{23,24,26}. Interestingly, alterations of 2'Ome have been observed in cancer and we recently demonstrated by profiling 195 primary mammary tumors using the RiboMethSeq approach, that only 40% of the known 2'O-methylated sites are altered, suggesting that only few rRNA sites can tolerate a lack of 2'Ome. Moreover, rRNA 2'Ome alterations are not random since rRNA 2'Ome profiles were associated with breast cancer subtypes and tumor grades²⁵. Similarly, alterations of rRNA 2'Ome were described in a cohort of 17 diffuse large B-cell lymphoma samples²⁷ and of 94 acute myeloid leukemia samples²⁸. Importantly, alterations of rRNA 2'Ome at some specific sites can affect both the translation of particular mRNA subsets and cell proliferation^{15,23,24,26 29,30}. To date, whether alterations of rRNA epitranscriptomics occurs in gliomas and contributes to disease etiology remains unexplored. Here, we investigated whether IDHwt and IDHmut HGGs display alterations in ribosome biology, in terms of rRNA epitranscriptomics and ribosome biogenesis, to exploit these features as novel therapeutic targets of these diseases.

Materials and methods

Human grade 3-4 adult-type diffuse glioma and non-neoplastic samples

Three cohorts were built: a technical cohort (8 grade 4 IDHwt glioblastomas, 3 non-tumoral samples); a test cohort detailed in Table 1 (13 IDHwt glioblastomas, 13 IDHmut astrocytomas, 14 IDHmut and 1p/19q codeleted oligodendrogliomas, 6 non-tumoral samples); a validation cohort (9 IDHwt glioblastomas, 6 IDHmut astrocytomas, 8 IDHmut and 1p/19q co-deleted oligodendrogliomas). The percentage of tumoral cells was estimated by a neuropathologist as described in Fig.S1. Additional details are provided in Supplementary Information.

Cell culture

Human IDHwt glioblastoma (5706, N131520), IDHmut astrocytoma (LGG85) and IDHmut and 1p/19q codeleted oligodendroglioma (BT138, BT237) cells were cultured as spheres as described in Supplementary Information.

Reverse Transcription and real time quantitative PCR

cDNA synthesis was performed using the Prime Script RT Reagent kit (Takara). Medium throughput qPCR was performed using the Biomark HD system (Fluidigm) as previously described³¹ (Table S1). The median Ct value of 5 housekeeping mRNAs was used for normalization.

RiboMethSeq

RiboMeth-seq was performed as previously described using the Illumina sequencing technology^{25,32}. To process the sequencing data, a novel nextflow pipeline RiboMethSeq-nf was developed and is currently available (<https://github.com/RibosomeCRCL/ribomethseq-nf>). This pipeline processes sequencing data as previously described^{25,32,33}. To calculate the C-score, which reflects the rRNA 2'Ome level, the novel R package rRMSAnalyzer was developed (<https://github.com/RibosomeCRCL/rRMSAnalyzer>). The identification of significant alterations in rRNA 2'Ome levels between groups was performed by applying two consecutive thresholds: the adjusted p-value < 0.05 (Kruskal-Wallis with FDR adjustment); and the mean Δ C-score (*i.e.*, difference between the highest and lowest mean C-score of the groups of interest) > 0.05.

IC₅₀ assay

3.10³ cell spheroids were treated with CX5461 (Sigma-Aldrich)³⁴ or BMH-21 (Sigma-Aldrich)¹⁰. Cell cytotoxicity was assessed by CellTox™ Green Cytotoxicity Assay (Promega) and by CellTiter-Glo3D® luminescent cell viability assay (Promega). Cell viability was expressed as a percentage of the signal intensity normalized against DMSO (1%).

Results

A standardized approach for large-scale analyses of human samples using RiboMethSeq

Before investigating alterations of rRNA 2'Ome in the three main histomolecular HGGs, we first optimized the recently described RiboMethSeq approach^{25,32,35} to determine reliable quantifications of 2'Ome levels at 106 rRNA sites from patient tumor samples. First, based on the technical cohort (n=11) of IDHwt glioblastomas and non-neoplastic tissues, we observed that the C-score, which reflects rRNA 2'Ome levels at specific sites, was similar using either a manual or an automated RNA extraction protocol (Fig.S2). Second, we used the NovaSeq Illumina sequencing platform (up to 10 billion reads) to increase the total number of useful reads (Fig.S3A) and the number of samples sequenced in a single flowcell.

We then randomly separated RNA samples of the test cohort and prepared two independent libraries of 23 samples (40 HGGs and 6 non-neoplastic samples), each library also contained a commercially-available "reference" total RNA. Unsupervised analysis of the entire test cohort using PCA based on C-scores of either all rRNA positions (7055 sites) or the 106 positions corresponding to known rRNA 2'Ome sites, clearly distinguished samples depending on the library of origin, as illustrated by the lack of clustering of reference RNA (Fig. S3B, left panels). We evaluated adjustment of RiboMethSeq data using the ComBat-seq algorithm, one of the most routinely used tools to adjust RNA-seq data³⁶. Upon ComBat-seq adjustment, no distinction between samples based on their library of origin was observed in C-scores, including for the two reference RNA (Fig.S3B, right panels). These data demonstrate the efficacy of the ComBat-seq algorithm at removing batch effect from RiboMethSeq data.

Based on these results, we developed bioinformatics tools to perform reproducible analyses of RiboMethSeq data arising from large-scale cohorts (<https://github.com/RibosomeCRCL>).

rRNA 2'Ome profiles discriminate IDHwt from IDHmut adult-type diffuse gliomas

Using the optimized approach selected above, we then investigated whether alterations of rRNA 2'Ome differentially occur in the three main histomolecular HGGs using the test cohort: IDHwt glioblastoma (G, n=13), IDHmut astrocytoma (A, n=13), IDHmut and 1p19q codeleted oligodendroglioma (O, n=14) and non-neoplastic cerebral cortex (NT, n=6) (Table 1). Using unsupervised hierarchical clustering analysis (HCA), we first evaluated rRNA 2'Ome levels at the 106 known sites in the 46 non-neoplastic and glioma samples (Fig.1). The C-score reflects the rRNA 2'Ome levels as it corresponds to the ratio of the 5' read-end counts at a nucleotide position to the local 5' read-end count coverage; and when close to 1, C-score indicates that all rRNA molecules of the sample are 2'O-methylated at this specific site; whereas a C-score below 0.9 reflects a mix of 2'O-unmethylated and 2'O-methylated rRNA molecules. Here, most rRNA 2'Ome sites had a score close to 1, albeit some sites were below 0.9, substantiating recent results in human samples from diffuse large B cell lymphoma, acute myeloid leukemia and breast cancer^{25,27,28}. These data further confirmed observations by us and others that some rRNA molecules exist without 2'Ome at some specific sites, including in non-neoplastic tissue.

Interestingly, all IDHwt glioblastoma samples formed a separate branch (left-hand side of the HCA dendrogram), suggesting that their rRNA 2'Ome profile was clearly different from IDHmut astrocytoma and oligodendroglioma, as well as from non-neoplastic tissue (Fig.1). Principal Component Analyses (PCAs) based on the rRNA 2'Ome profile indicated that the PC2 axis (variance=14.1%) strongly differentiated glioblastomas from other samples (Fig.S4A). To ensure consistency between the results of our classification and the expected outcome of the patients, we correlated PCA axes with survivals and mitotic index, as an internal control of tumor sample classification. Consistent with the known differences regarding glioblastomas and IDHmt HGGs characteristics, PC2 was significantly correlated with the *IDH1/2* mutational status, the mitotic index, overall survival (OS) and progression-free survival (PFS) (Fig.S4B-D). To validate these observations, we analyzed rRNA 2'Ome levels using RiboMethSeq on the

technical cohort, corresponding to an independent cohort composed of 8 IDHwt glioblastomas and 3 non-neoplastic tissues. Unsupervised PCA based on the rRNA 2'Ome profile showed that IDHwt glioblastomas could once again be clearly separated from non-neoplastic tissues (Fig.S4E). Altogether, our data revealed that rRNA 2'Ome levels vary in HGGs as well as in non-neoplastic cerebral cortex, and that rRNA 2'Ome profiles discriminate IDHwt glioblastomas not only from non-neoplastic tissues but also from IDHmut HGG types.

Most variable rRNA 2'Ome sites are sufficient to discriminate IDHwt glioblastoma from IDHmut adult-type diffuse gliomas

To better characterize differences in rRNA 2'Ome profiles between histomolecular HGG types, we then focused on the most variable rRNA 2'Ome sites. To identify such sites, we compared the variability of C-scores at each single site among all HGG samples of the test cohort (n=40) using the distribution of the inter-quartile range (IQR). A set of 19 sites showed an IQR higher than median + 2 × median absolute deviation (mad) and were considered as the most variable rRNA 2'Ome sites among HGGs (red, Fig.2A), in agreement with our recent findings that only a subset of rRNA sites displays variability in 2'Ome levels²⁵. Interestingly, PCAs indicated that rRNA 2'Ome profiles based on this set of 19 sites are sufficient to discriminate IDHwt glioblastomas, IDHmut astrocytoma and oligodendrogliomas (Fig.2B).

To validate these observations, we used a second, independent validation cohort of 23 HGG samples (9 IDHwt glioblastomas, 6 IDHmut astrocytomas and 8 IDHmut, 1p/19q codeleted oligodendrogliomas) (Fig.S1B). We performed an unsupervised analysis using the 19 most variable rRNA 2'Ome sites identified using the test cohort (Fig.2A). As for the test cohort, unsupervised analyses of the validation cohort distinguished the three histomolecular subtypes of HGGs (Fig.2C). In addition, the projection of the validation cohort samples onto the PCA constructed from the test cohort enabled us to identify the histomolecular subtypes of each sample, suggesting that *de novo* profiling of rRNA 2'Ome could help in the classification of HGGs (Fig.2D). In addition, comparison of test and validation cohorts in term of percentage of tumor cells suggests that the tumor heterogeneity did not affect our conclusions (Fig. S1B). Indeed, in the validation cohort, the mean percentage of tumor cells is significantly lower in astrocytomas (38%) compared to oligodendrogliomas (69%), while no difference was observed with glioblastomas (9%) (Kruskal-Wallis: p=0.045*; Mann-Whitney: A vs O

p=0.024*). In contrast, in the test cohort, the mean percentage of tumor cells is significantly lower in astrocytomas (38%) and oligodendrogliomas (39%) compared to glioblastomas (55%) (Kruskal-Wallis: p=0.034*; Mann-Whitney: A vs G p=0.0172*; O vs G p=0.0348*).

These data further emphasize the specificity of IDHwt glioblastoma rRNA 2'Ome profiles compared to IDHmut HGGs and suggest that IDHwt glioblastomas display strong alterations of rRNA 2'Ome levels at some specific sites.

Glioblastomas display the most frequent site-specific rRNA 2'Ome alterations

To identify rRNA sites whose 2'Ome levels significantly differed between HGG histomolecular types and non-neoplastic tissues, we performed a systematic analysis of each of the 106 rRNA 2'Ome sites using the test cohort and applied two consecutive thresholds, a Kruskal-Wallis test with adjusted p-values < 0.05 and a cut-off value for mean ΔC -scores_{max-min} > 0.05. From this screen, only 16 rRNA 2'Ome sites displayed a significant variation in their level of methylation in at least one HGG or non-neoplastic tissue (Fig.3). Pairwise comparisons for these 16 sites revealed that 4 and 6 sites displayed significant alterations in 2'Ome levels in high-grade astrocytomas and high-grade oligodendrogliomas, respectively, compared to non-neoplastic tissues (Fig.3B). In addition, rRNA 2'Ome levels appeared to be significantly increased on 6 sites in high-grade astrocytomas compared to high-grade oligodendrogliomas. Similar alterations in rRNA 2'Ome levels between IDHwt and IDHmut tumours were observed using the validation cohort (Fig.S5A). Finally, the main differences could be attributed to glioblastomas that displayed 12 and 14 of the 16 rRNA sites significantly altered compared to non-neoplastic samples or high-grade astrocytoma and oligodendrogliomas, respectively. Strikingly, rRNA 2'Ome levels were mostly lower in glioblastomas compared to non-neoplastic tissues, high-grade astrocytoma or high-grade oligodendrogliomas (Fig.3A). The same overall decrease in rRNA 2'Ome levels was confirmed in glioblastoma compared to non-neoplastic tissues using the technical cohort (Fig.S5B). Altogether, these results indicate that 2'Ome levels are altered at specific rRNA sites in HGGs, while glioblastomas display the highest frequency of alterations in rRNA 2'Ome levels compared to non-neoplastic cerebral cortex and other HGG histomolecular types.

Changes in C/D box snoRNA expression levels only partially explain alterations of rRNA 2'Ome levels

To investigate the origin of alterations of rRNA 2'Ome in HGGs, we focused on the expression of C/D snoRNAs (snoRDs), which guide in a sequence-specific manner the methyl-transferase FBL toward the rRNA nucleotide to methylate. We thus examined the correlation between levels of rRNA 2'Ome and related snoRDs. It was reported that snoRNA expression levels can be inferred from RiboMethSeq data^{37,38}. Thus, we used RiboMethSeq raw data from the NovaSeq platform and applied an in-house pipeline to overcome limitations of snoRNA analysis by next-generation sequencing (see Supplementary methods)^{39,40}. A strong and significant correlation (about 92%) between snoRNA levels either determined from RiboMethSeq or measured by RT-qPCR was observed in 9 glioma samples for 11 out of 12 selected snoRDs, thus validating our approach (Fig.S6A). Given that 2'Ome at a single rRNA site is catalyzed either by one or several snoRD^{15,41}, we restricted our analysis to the rRNA 2'Ome sites (n=46) guided by a single snoRD. No significant correlation was observed between levels of rRNA 2'Ome and of corresponding snoRDs among 37 sites (Fig.S6B). In contrast, a significant albeit relatively low positive correlation was observed for 9 pairs of snoRD/rRNA sites, the best correlation being that of the 18S-Am576 site and its associated SNORD93 ($\text{padj}=9.10^{-6}$, $r=0.68$) (Fig.S6B-C). Thus, alterations of rRNA 2'Ome levels cannot be exclusively attributed to changes in C/D box snoRNA expression levels.

The expression profile of ribosome biogenesis factors discriminates IDHmut and IDHwt HGGs

Since variations in snoRD expression levels cannot explain most of the changes observed in rRNA 2'Ome levels, we tested a novel hypothesis. Indeed, in cancer, variations of 2'Ome levels in rRNAs are believed to passively arise from the link between ribosome biogenesis (RiBi) and concomitant rRNA chemical modifications, whereby changes in ribosome synthesis impact the rate-limiting rRNA 2'Ome process and therefore influence 2'Ome profiles^{15,25,27}. Therefore, an overall decrease in rRNA 2'Ome levels observed in different cancer tissues may be caused by RiBi hyperactivation to sustain a high demand in protein synthesis necessary to support the highly proliferative cancer cells. As IDHwt glioblastomas possess a higher proliferative rate than IDHmut astrocytoma and oligodendrogliomas, including in our test cohort (based on

the mitotic index) (Fig.S4C-D), we hypothesized that the decrease in rRNA 2'Ome levels at specific positions in IDHwt glioblastomas could be due to a rate-limiting 2'Ome process caused by an exacerbated RiBi.

To investigate RiBi dysregulations across HGGs, we initially applied a gold-standard approach by analyzing levels of the 47S rRNA precursor (pre-rRNA), using Northern blot (Fig.S7A). However, this approach using tumor samples was challenging, notably due to the need for a large quantity of biological materials. Nevertheless, in a panel of 9 analyzable samples, IDHmut astrocytoma and oligodendrogliomas surprisingly seemed to express more pre-47S rRNAs than IDHwt glioblastomas. However, only two IDHwt glioblastoma samples were analyzed, therefore preventing us to draw any conclusion. To bypass this technical issue, we then measured the expression of a set of 20 genes involved in the early RiBi stages (referred to as "RiBi-gene set"). To reflect as much as possible this multistep process involving more than 200 factors⁷, we selected the RiBi-gene set implicated in the main RiBi process, including rRNA transcription (*NCL*, *NPM*, *POLR1A*, *TAF1A*, *TAF1B*, *TAF1C* and *UBTF*), rRNA maturation (*BOP1*, *PES1* and *WDR12*), snoRNA biogenesis (*RUVBL1*, *PIDH1D1* and *RUVBL2*), and H/ACA (*DKC1*, *GAR1*, *NHP2* and *NOP10*) and C/D box (*NOP56*, *SNU13* and *FBL*) snoRNP complexes (Fig.4A). Of note, three genes (*PIH1D1*, *RUVBL2* and *FBL*) are located on the long arm of chromosome 19 (19q), which undergoes a heterozygous deletion in high-grade oligodendrogliomas. A readout for RiBi at steady-state was determined by quantifying mRNA expression levels of these selected genes by medium throughput RT-qPCR in our validation series. mRNA levels were normalized against the median mRNA expression of 5 housekeeping genes, which did not significantly vary among the four groups (Fig.S7B).

To examine the association between expression levels of RiBi factors and HGGs, we first performed an unsupervised approach using a PCA based on the RiBi-gene set profile (Fig.4B). Interestingly, three main clusters were observed. A first large cluster, composed of both non-neoplastic tissues and IDHwt glioblastomas (NT/G cluster), was distinct from two other clusters corresponding to IDHmut oligodendrogliomas (O) and astrocytoma (A). PC1 (variance: 67.8%), in particular, separated the NT/G cluster from A/O clusters, while the PC2 (variance: 9%) distinguished the O cluster from others. These data suggest that the expression profile of only 20 RiBi factors discriminate HGGs.

To ensure consistency between the results of our classification and the expected outcome of the patients, we first calculated Pearson's correlation coefficients between the first 5 PC dimensions and OS or PFS as an internal control (Fig.4C and Fig.S7C). Consistently, we observed a significant association exclusively for PC1 and PC2, indicating that the clustering based on RiBi-gene set profiles provided by these two axes is sufficient to recapitulate all clinical data of interest. OS and PFS were significantly correlated with both PC1 and PC2 in a negative manner, indicating that samples clustering at the right-hand side of the PC1 and top of PC2, *i.e.*, IDHwt glioblastomas, display lower OS and PFS. Indeed, IDHwt glioblastoma patients exhibit the poorest OS (less than 30 months) and PFS (under 30 months), followed by IDHmut astrocytoma and oligodendroglioma patients that tend to cluster at the left part of PC1 and the top or bottom part of PC2, respectively.

Strikingly, we also identified a strong correlation between PC1 and PC2 axes, and the *IDH1/2* mutational and 1p/19q co-deletion status, respectively (Fig.S7D-E). Indeed, PC1 (G vs. A/O clusters) was significantly correlated with the *IDH1/2* mutational status while PC2 (A/G vs. O clusters) segregated HGG tumors based on the 1p/19q co-deletion status. Thus, expression profiling of the RiBi-gene set was strongly correlated with both clinical features and distinct genomic alterations of the HGG test cohort. Altogether, these results suggest that the expression signature of only 20 genes involved in ribosome biogenesis is sufficient to discriminate IDHwt from IDHmut HGG histomolecular types and that RiBi displays IDH mutational status-dependent alterations.

Ribosome biogenesis factors are highly expressed in IDHmut adult-type diffuse gliomas

Next, we individually compared mRNA expression levels of the 20 RiBi factors among the different HGGs (Fig.5 and Fig.S8A). Significant differences were observed in the expression of all tested RiBi factors between different groups (Mann Whitney test, Fig.S8A). Surprisingly, only a few RiBi genes were significantly differentially expressed in IDHwt glioblastomas compared to non-neoplastic samples (9 out of 20), with very moderate changes (≤ 2 -fold change). In contrast, IDHmut astrocytoma and oligodendrogliomas significantly overexpressed most of these RiBi genes (19 and 16 out of 20 RiBi genes, respectively). For instance, expression of *NCL*, which encodes a key factor in rRNA synthesis, increased by 2- and 3-fold in IDHmut astrocytoma and oligodendrogliomas, respectively ($p < 0.001$), while *NCL* expression levels in IDHwt samples

only slightly increased (Fig.5A and Fig.S8A). Likewise, the use of a second distinct set of primers to analyze *NCL* expression provided the exact same trend (Fig.S8B), therefore ruling out a potential technical caveat. These results suggest that ribosome biogenesis could be enhanced in IDHmut astrocytoma and oligodendrogliomas compared to IDHwt glioblastomas and non-neoplastic tissues.

Interestingly, genes located on chromosome 19q (*FBL*, *PIH1D1*, *RUVBL2*) displayed a particular expression pattern (Fig.5C, 5E and Fig.S7E). Like other genes involved in RiBi, *FBL*, *PIH1D1* and *RUVBL2* were significantly overexpressed in IDHmut astrocytomas compared to both IDHwt glioblastomas and non-neoplastic samples. However, mRNA expression levels in IDHmut oligodendrogliomas were lower than in IDHmut astrocytomas and displayed expression profiles resembling those of IDHwt glioblastomas. Thus, *FBL* was highly expressed exclusively in IDHmut astrocytomas, whereas its expression levels were equivalent in IDHmut oligodendrogliomas and IDHwt glioblastomas, as confirmed by a second set of primers (Fig.S8B). Considering that IDHmut oligodendroglioma samples exhibited a heterozygous deletion of *FBL*, *PIH1D1* and *RUVBL2* genes located on 1p/19q chromosomes, these data indicate that the specific expression profile observed for these genes in IDHmut oligodendrogliomas is likely due to a haploinsufficiency caused by genetic alterations. Interestingly, removal of these three genes in the RiBi-genes set still allowed us to distinguish IDHwt from IDHmut HGGs (data not shown), suggesting that copy number variation (CNVs) affecting RiBi gene expression does not impact the distinction between IDHwt and IDHmut, as expected. Therefore, the ribosome biogenesis pathway is strongly enhanced in IDHmut gliomas, *i.e.*, high-grade astrocytoma and oligodendroglioma, but remains moderately affected in IDHwt glioblastoma.

HGGs display distinct cytotoxicity to RNA pol I inhibitors CX5461 and BMH-21

Having identified an IDH mutational status-dependent alteration of RiBi in HGGs, we hypothesized that IDHmut and IDHwt HGGs display distinct cytotoxicity to RNA Pol I inhibitors, BMH-21 and CX5461, which inhibit the transcription of the 47S pre-rRNA and are promising new cancer treatments. We used a panel of 5 representative HGG cell lines, comprising IDHmut astrocytoma and IDHmut and 1p/19q codeleted oligodendroglioma cell lines (LGG85 and BT138/237, respectively) and IDHwt glioblastoma cell lines (5706 and N131520). Analyses of HGG spheroids in response to 72-

hour treatments with RNA pol I inhibitors showed that all spheroids were similarly sensitive to BMH-21 with an IC_{50} ranging from 1.06 to 1.56 μ M (Fig.6A-C), as recently observed⁴². However, CX5461 strongly impacted the viability of IDHmut astrocytoma and oligodendroglioma spheroids (IC_{50} ranging from 5.92 to 7.55 μ M), but not of IDHwt glioblastoma spheroids (Fig.6D-F). Hence, these results are consistent with our previous findings that IDHmut astrocytomas and oligodendrogliomas may be addicted to an enhanced RiBi pathway, therefore potentially sensitizing these AGD histomolecular types to clinically available RiBi inhibitors. Altogether, our results highlight the potency of RNA Pol I inhibitor usage as potential HGG therapy and further support an over-activation of the RiBi pathway in IDHmut astrocytomas and oligodendrogliomas compared to IDHwt glioblastomas and non-neoplastic tissues.

Discussion

High-grade adult-type diffuse gliomas (HGGs) are heterogeneous tumors associated with distinct, albeit poor, survival rates due to the lack of effective targeted therapies, in particular for the most aggressive histomolecular type, the IDHwt glioblastoma. Here, by performing the first concomitant analysis of rRNA 2'Ome and ribosome biogenesis in primary tumors, we report distinct, uncoupled alterations of rRNA epitran-scriptomics and ribosome biogenesis in IDHmut and IDHwt HGGs, therefore revealing specific dysregulations of the ribosome biology that constitute new IDH mutational status-associated hallmarks of HGGs.

In the last 7 years, alterations of rRNA 2'Ome profiles have been reported using a newly developed approach RiboMethSeq in numerous cellular models and only in three types of cancers, namely breast cancer, acute myeloid leukemia and diffuse large-B cell lymphoma (DLBCL)^{15,25,27,28}. Such alterations have been shown to be restricted to only 40% of the known rRNA 2'Ome sites, suggesting that only one third of the sites may possess regulatory functions on ribosome activity. We now show that rRNA 2'Ome profiles also vary in HGGs. As previously observed in other cancers, only a small subset of known rRNA 2'Ome sites display variability in their 2'Ome levels in HGGs, suggesting these positions can tolerate absence of 2'Ome. The 19 most variable rRNA 2'Ome sites were randomly distributed on the ribosome structure, suggesting no coordinated effects on functional domains of the ribosome. Notably, similar increases in rRNA 2'Ome levels at 18S_Am576 and decreases at 18S_Gm1447 were

observed in the most aggressive HGG type, glioblastoma, and breast cancer subtypes (triple negative or TNBC), suggesting a link between these sites and cancer aggressiveness²⁵. A recent study demonstrated that alterations of 2'Ome levels at a single rRNA site are sufficient to affect cell proliferation, a hallmark of cancer aggressiveness²⁶. Moreover, rRNA 2'Ome at 18S_Gm1447 was recently shown to support leukemic stem cell functions by modulating translation²⁸. Hence, whether these rRNA 2'Ome sites common to both HGGs and breast cancer contribute to the acquisition of cancer cell characteristics remains to be deciphered and could potentially represent new targetable vulnerabilities.

In IDHwt glioblastomas, alterations in rRNA 2'Ome levels mostly correspond to a decrease as observed in both the test and validation cohorts. In DLBCL, the global decrease in rRNA 2'Ome levels was correlated with the Ki67-estimated high proliferative rate of tumors. One hypothesis was that low rRNA 2'Ome levels indirectly resulted from an increase in rRNA synthesis associated with the hyperproliferative rate of cancer cells, which rendered components of the rRNA 2'Ome machinery limiting, although rRNA synthesis was not analyzed²⁷. Consistently, we observed specific alterations of rRNA 2'Ome in IDHwt glioblastomas, which are the most proliferative tumors and display the highest mitotic index in our test cohort. However, we surprisingly observed an elevated ribosome biogenesis in IDHmut astrocytomas and oligodendrogliomas compared to glioblastomas, suggesting that RiBi levels are not correlated with the proliferative rate, at least in HGGs, and cannot solely explain alterations of rRNA epitranscriptomics in HGGs. Even though the rate of ribosome biogenesis may contribute to regulating rRNA 2'Ome through a passive effect, additional molecular mechanisms should be further explored to identify the origin of rRNA 2'Ome alterations in cancer and understand the observed rRNA site- and cancer type-specificity. The mechanisms may include alterations of expressions and/or activities of RNA-binding proteins, such as DDX21 and FMRP, which contribute to the formation of *bona fide* functional snoRNP complexes^{29,43}. Here, we report that alterations of C/D box snoRNA expression could be sufficient to explain alterations of rRNA 2'Ome levels at some, but not all, rRNA sites. The evolution of annotation and/or knowledge in biology of C/D box snoRNAs may fill the gap to better understand causes of rRNA 2'Ome alterations in cancer. Altogether, our findings that main HGG histomolecular types are associated with alterations in either ribosome quantity or quality, challenge the hypothesis that the decrease

in rRNA 2'Ome levels mainly results from a passive effect caused by an exacerbated ribosome biogenesis.

Our data reveal that IDHmut HGGs, including both high-grade astrocytoma and oligodendroglioma, display the highest expression of ribosome biogenesis factors, suggesting an increase in ribosome biogenesis. Whether dysregulations of *IDH1/2* functions, notably through the production of the oncometabolite D-2-hydroxyglutarate, could directly impact the regulation of ribosome biogenesis would need to be further explored. Nevertheless, the specificity of ribosome biogenesis alterations in HGGs offers novel perspectives for clinical applications. Building on our observations, we found that HGGs are sensitive to the newly developed RNA pol I inhibitors, CX5461 and BMH-21, the former being successfully evaluated in clinical trials in advanced solid and hematological cancers⁷. Sensitivity of HGGs to RNA pol I inhibitors CX5461 and BMH-21 has already been reported^{42,44,45}, even though discrepancies regarding the sensitivity of glioblastomas to CX5461 exist between our data and previous ones, possibly due to differences in experimental settings and genetic backgrounds of tested cell lines. In particular, the 3D culture conditions could decrease drug sensitivity compared to 2D culture conditions, as already reported⁴⁶. In addition, the differential sensitivity of glioblastomas to CX5461 and BMH-21 could be attributed to off-target effects of these molecules as these RNA Pol I inhibitors act through distinct mechanisms and are known to affect several cellular pathways, including DNA repair^{10,34,47}. Thus, whether the activity of these compounds may also rely on the genetic background of tested models impacting the different sensitivities of HGG types to CX5461 and BMH-21, should be further investigated.

Altogether, our data indicate that alterations of the ribosome biology in HGGs are dependent on the IDH mutational status and could represent targetable features in clinic. Thus, recent discoveries in the field of ribosomes have opened new avenues not only for a better understanding of cellular processes that contribute to HGG development and aggressiveness but also for designing future HGG type-specific therapeutic strategies.

Conflict of interest

The authors have no conflicts of interest to declare.

Ethical Approval

All the experiment protocol for involving human was in accordance with the guidelines of French regulation. Written informed consent was obtained from all patients.

Fundings

This work was supported by INCa (PLBio 2019-138 MARACAS), the French Association pour la Recherche sur les Tumeurs Cérébrales (ARTC), the Cancéropôle Lyon Auvergne Rhône-Alpes (AAP international 2021 MARACAS.v3.0), the Ligue Contre le Cancer Auvergne-Rhône-Alpes and the SIRIC program (INCa-DGOS-Inserm_12563, LyRICAN). HP and NEHM were recipients of PhD fellowships from Ligue Nationale Contre le Cancer. JH was recipient of PhD fellowship from French Minister of Research.

Author contribution

HP, NEHM, SB, JH, FB, VA, MC, JP, DB, LCV, SD performed and analysed experiments. HP, NEHM, JK, ET, DB performed statistical descriptions and bioinformatic analyses. HP, TC, AF, JK, ET, LT, AV developed bioinformatic tools. LCV, EH, MS provided cell lines. DM, FD provided human samples and clinical data. AF, JK, ET, VA, SG, MSS, EH, MS, DM, FC, VM, SB supervised experimental process. HP, NEHM, SB, JK, SG, FD, VM and SD interpreted the data. VM and SD shaped the clinical and research question and supervised the project coordination. AV, MSS, EH, MS, MG, JJD, FD, VM and SD provided financial supports. HP, NEHM, VM and SD wrote the first draft of the manuscript. All authors have read and approved the manuscript.

Availability of datasets

The generated RiboMethSeq data are available in the GEO profile (GSE224104, token for reviewer access: qhabqswmfzotlwh). The datasets include the fastq of each sample, a C-score matrix for each cohort after batch effect adjustment using ComBat-seq and a matrix summarizing the clinical data.

Acknowledgements

We would like to thank all the people involved in this study, including the patients and their families. We thank Drs A Idbaih (ICM, Paris, France), JP Hugnot (IGF, Montpellier, France) and K Ligon (Brigham and Women's Hospital, Boston, USA) for generously providing cell lines. We thank platform staffs that have not been referred as co-authors: NeuroBioTec (CRB HCL, Lyon, France, Biobank BB-0033-00046); Organoid platform (CRCL, Lyon, France); Gilles Thomas Bioinformatic platform (CRCL, Lyon, France); Cancer Genomic platform (CRCL, Lyon, France). The manuscript has been edited by Brigitte Manship (CRCL, Lyon, France).

References

1. Wen PY, Weller M, Lee EQ, et al. Glioblastoma in adults: a Society for Neuro-Oncology (SNO) and European Society of Neuro-Oncology (EANO) consensus review on current management and future directions. *Neuro Oncol.* 2020;22(8):1073-1113. doi:10.1093/NEUONC/NOAA106
2. Lapointe S, Perry A, Butowski NA. Primary brain tumours in adults. *Lancet.* 2018;392(10145):432-446. doi:10.1016/S0140-6736(18)30990-5
3. Lassman AB, Hoang-Xuan K, Polley MYC, et al. Joint Final Report of EORTC 26951 and RTOG 9402: Phase III Trials With Procarbazine, Lomustine, and Vincristine Chemotherapy for Anaplastic Oligodendroglial Tumors. *J Clin Oncol.* 2022;40(23):2539-2545. doi:10.1200/JCO.21.02543
4. van den Bent MJ, Tesileanu CMS, Wick W, et al. Adjuvant and concurrent temozolomide for 1p/19q non-co-deleted anaplastic glioma (CATNON; EORTC study 26053-22054): second interim analysis of a randomised, open-label, phase 3 study. *Lancet Oncol.* 2021;22(6):813-823. doi:10.1016/S1470-2045(21)00090-5
5. Bastide A, David A. The ribosome, (slow) beating heart of cancer (stem) cell. *Oncogenesis* 2018 7:4. 2018;7(4):1-13. doi:10.1038/s41389-018-0044-8
6. Barna M, Pusic A, Zollo O, et al. Suppression of Myc oncogenic activity by ribosomal protein haploinsufficiency. *Nature* 2008 456:7224. 2008;456(7224):971-975. doi:10.1038/nature07449
7. Catez F, Dalla Venezia N, Marcel V, Zorbas C, Lafontaine DLJ, Diaz JJ. Ribosome biogenesis: An emerging druggable pathway for cancer therapeutics. *Biochem Pharmacol.* 2019;159:74-81. doi:10.1016/J.BCP.2018.11.014
8. Penzo M, Montanaro L, Treré D, Derenzini M. The Ribosome Biogenesis—Cancer Connection. *Cells* 2019, Vol 8, Page 55. 2019;8(1):55. doi:10.3390/CELLS8010055
9. Bywater MJ, Poortinga G, Sanij E, et al. Inhibition of RNA Polymerase I as a Therapeutic Strategy to Promote Cancer-Specific Activation of p53. *Cancer Cell.* 2012;22(1):51-65. doi:10.1016/J.CCR.2012.05.019
10. Peltonen K, Colis L, Liu H, et al. A targeting modality for destruction of RNA polymerase I that possesses anticancer activity. *Cancer Cell.* 2014;25(1):77-90. doi:10.1016/J.CCR.2013.12.009
11. Hilton J, Gelmon K, Bedard PL, et al. Results of the phase I CCTG IND.231 trial of CX-5461 in patients with advanced solid tumors enriched for DNA-repair deficiencies.

- 653 *Nature Communications* 2022 13:1. 2022;13(1):1-12. doi:10.1038/s41467-022-31199-
654 2
- 655 12. Khot A, Brajanovski N, Cameron DP, et al. First-in-human RNA polymerase I tran-
656 scription inhibitor CX-5461 in patients with advanced hematologic cancers: Results of
657 a phase I dose-escalation study. *Cancer Discov.* 2019;9(8):1036-1049.
658 doi:10.1158/2159-8290.CD-18-1455/333397/AM/FIRST-IN-HUMAN-RNA-POLY-
659 MERASE-I-TRANSCRIPTION
- 660 13. Xu H, Di Antonio M, McKinney S, et al. CX-5461 is a DNA G-quadruplex stabilizer
661 with selective lethality in BRCA1/2 deficient tumours. *Nature Communications* 2017
662 8:1. 2017;8(1):1-18. doi:10.1038/ncomms14432
- 663 14. Marcel V, Catez F, Diaz JJ. Ribosome heterogeneity in tumorigenesis: the rRNA point
664 of view. *Mol Cell Oncol.* 2015;2(3). doi:10.4161/23723556.2014.983755
- 665 15. Jaafar M, Paraqindes H, Gabut M, Diaz JJ, Marcel V, Durand S. 2'O-Ribose Methyla-
666 tion of Ribosomal RNAs: Natural Diversity in Living Organisms, Biological Processes,
667 and Diseases. *Cells* 2021, Vol 10, Page 1948. 2021;10(8):1948.
668 doi:10.3390/CELLS10081948
- 669 16. Miller SC, MacDonald CC, Kellogg MK, Karamysheva ZN, Karamyshev AL. Special-
670 ized Ribosomes in Health and Disease. *International Journal of Molecular Sciences*
671 2023, Vol 24, Page 6334. 2023;24(7):6334. doi:10.3390/IJMS24076334
- 672 17. Xue S, Barna M. Specialized ribosomes: a new frontier in gene regulation and organis-
673 mal biology. *Nature Reviews Molecular Cell Biology* 2012 13:6. 2012;13(6):355-369.
674 doi:10.1038/nrm3359
- 675 18. Genuth NR, Barna M. Heterogeneity and specialized functions of translation machin-
676 ery: from genes to organisms. *Nature Reviews Genetics* 2018 19:7. 2018;19(7):431-
677 452. doi:10.1038/s41576-018-0008-z
- 678 19. Larionova TD, Bastola S, Aksinina TE, et al. Alternative RNA splicing modulates ribo-
679 somal composition and determines the spatial phenotype of glioblastoma cells. *Nat Cell*
680 *Biol.* 2022;24(10):1541-1557. doi:10.1038/S41556-022-00994-W
- 681 20. Gabut M, Bourdelais F, Cells SD, 2020 undefined. Ribosome and translational control
682 in stem cells. *mdpi.com.* 2020;9(2). doi:10.3390/cells9020497
- 683 21. Shirakawa Y, Hide T, Yamaoka M, et al. Ribosomal protein S6 promotes stem-like
684 characters in glioma cells. *Cancer Sci.* 2020;111(6):2041-2051.
685 doi:10.1111/CAS.14399
- 686 22. Hide T, Shibahara I, Inukai M, Shigeeda R, Kumabe T. Ribosomes and Ribosomal Pro-
687 teins Promote Plasticity and Stemness Induction in Glioma Cells via Reprogramming.
688 *Cells* 2022, Vol 11, Page 2142. 2022;11(14):2142. doi:10.3390/CELLS11142142
- 689 23. Erales J, Marchand V, Panthu B, et al. Evidence for rRNA 2'-O-methylation plasticity:
690 Control of intrinsic translational capabilities of human ribosomes. *Proc Natl Acad Sci*
691 *U S A.* 2017;114(49):12934-12939.
692 doi:10.1073/PNAS.1707674114/SUPPL_FILE/PNAS.1707674114.SD03.XLSX
- 693 24. Marcel V, Ghayad SE, Belin S, et al. P53 Acts as a Safeguard of Translational Control
694 by Regulating Fibrillarin and rRNA Methylation in Cancer. *Cancer Cell.*
695 2013;24(3):318-330. doi:10.1016/J.CCR.2013.08.013
- 696 25. Marcel V, Kielbassa J, Marchand V, et al. Ribosomal RNA 2'O-methylation as a novel
697 layer of inter-tumour heterogeneity in breast cancer. *NAR Cancer.* 2020;2(4).
698 doi:10.1093/NARCAN/ZCAA036
- 699 26. Jansson MD, Häfner SJ, Altinel K, et al. Regulation of translation by site-specific ribo-
700 somal RNA methylation. *Nature Structural & Molecular Biology* 2021 28:11.
701 2021;28(11):889-899. doi:10.1038/s41594-021-00669-4

27. Krogh N, Asmar F, Côme C, Munch-Petersen HF, Grønbaek K, Nielsen H. Profiling of ribose methylations in ribosomal RNA from diffuse large B-cell lymphoma patients for evaluation of ribosomes as drug targets. *NAR Cancer*. 2020;2(4). doi:10.1093/NAR-CAN/ZCAA035
28. Zhou F, Aroua N, Liu Y, et al. A Dynamic rRNA Ribomethylome Drives Stemness in Acute Myeloid Leukemia. *Cancer Discov*. 2022;13:OF1-OF17. doi:10.1158/2159-8290.CD-22-0210
29. Zhou F, Liu Y, Rohde C, et al. AML1-ETO requires enhanced C/D box snoRNA/RNP formation to induce self-renewal and leukaemia. *Nat Cell Biol*. 2017;19(7):844-855. doi:10.1038/NCB3563
30. Nachmani D, Bothmer AH, Grisendi S, et al. Germline NPM1 mutations lead to altered rRNA 2'-O-methylation and cause dyskeratosis congenita. *Nat Genet*. 2019;51(10):1518-1529. doi:10.1038/S41588-019-0502-Z
31. Nguyen Van Long F, Lardy-Cleaud A, Carène D, et al. Low level of Fibrillarin, a ribosome biogenesis factor, is a new independent marker of poor outcome in breast cancer. *BMC Cancer*. 2022;22(1):1-12. doi:10.1186/S12885-022-09552-X/FIGURES/3
32. Marchand V, Ayadi L, el Hajj A, Blanloeil-Oillo F, Helm M, Motorin Y. High-Throughput Mapping of 2'-O-Me Residues in RNA Using Next-Generation Sequencing (Illumina RiboMethSeq Protocol). *Methods Mol Biol*. 2017;1562:171-187. doi:10.1007/978-1-4939-6807-7_12
33. Pichot F, Marchand V, Ayadi L, Bourguignon-Igel V, Helm M, Motorin Y. Holistic Optimization of Bioinformatic Analysis Pipeline for Detection and Quantification of 2'-O-Methylations in RNA by RiboMethSeq. *Front Genet*. 2020;11:38. doi:10.3389/FGENE.2020.00038/BIBTEX
34. Drygin D, Lin A, Bliesath J, et al. Targeting RNA polymerase I with an oral small molecule CX-5461 inhibits ribosomal RNA synthesis and solid tumor growth. *Cancer Res*. 2011;71(4):1418-1430. doi:10.1158/0008-5472.CAN-10-1728
35. Birkedal U, Christensen-Dalsgaard M, Krogh N, Sabarinathan R, Gorodkin J, Nielsen H. Profiling of ribose methylations in RNA by high-throughput sequencing. *Angew Chem Int Ed Engl*. 2015;54(2):451-455. doi:10.1002/ANIE.201408362
36. Zhang Y, Parmigiani G, Johnson WE. ComBat-seq: batch effect adjustment for RNA-seq count data. *NAR Genom Bioinform*. 2020;2(3). doi:10.1093/NARGAB/LQAA078
37. Sharma S, Marchand V, Motorin Y, Lafontaine DLJ. Identification of sites of 2'-O-methylation vulnerability in human ribosomal RNAs by systematic mapping. *Sci Rep*. 2017;7(1). doi:10.1038/S41598-017-09734-9
38. Delhermite J, Tafforeau L, Sharma S, et al. Systematic mapping of rRNA 2'-O methylation during frog development and involvement of the methyltransferase Fibrillarin in eye and craniofacial development in *Xenopus laevis*. *PLoS Genet*. 2022;18(1):e1010012. doi:10.1371/JOURNAL.PGEN.1010012
39. Deschamps-Francoeur G, Boivin V, Abou Elela S, Scott MS. CoCo: RNA-seq read assignment correction for nested genes and multimapped reads. *Bioinformatics*. 2019;35(23):5039-5047. doi:10.1093/BIOINFORMATICS/BTZ433
40. Bergeron D, Laforest C, Carpentier S, et al. SnoRNA copy regulation affects family size, genomic location and family abundance levels. *BMC Genomics*. 2021;22(1). doi:10.1186/S12864-021-07757-1
41. Bergeron D, Paraquindes H, Fafard-Couture É, et al. snoDB 2.0: an enhanced interactive database, specializing in human snoRNAs. *Nucleic Acids Res*. 2023;51(D1):D291-D296. doi:10.1093/NAR/GKAC835

- 750 42. Zisi A, Kanellis DC, Moussaud S, et al. Small Molecule-mediated Disruption of Ribo-
751 some Biogenesis Synergizes With FGFR Inhibitors to Suppress Glioma Cell Growth.
752 *Neuro Oncol*. Published online December 30, 2022. doi:10.1093/NEUONC/NOAC286
- 753 43. D'Souza MN, Gowda NKC, Tiwari V, et al. FMRP Interacts with C/D Box snoRNA in
754 the Nucleus and Regulates Ribosomal RNA Methylation. *iScience*. 2018;9:399-411.
755 doi:10.1016/J.ISCI.2018.11.007
- 756 44. Li G, Shen J, Cao J, et al. Alternative splicing of human telomerase reverse transcrip-
757 tase in gliomas and its modulation mediated by CX-5461. *Journal of Experimental and*
758 *Clinical Cancer Research*. 2018;37(1):1-13. doi:10.1186/S13046-018-0749-8/FIG-
759 URES/7
- 760 45. Chiu YC, Chen HIH, Zhang T, et al. Predicting drug response of tumors from inte-
761 grated genomic profiles by deep neural networks. *BMC Med Genomics*.
762 2019;12(1):143-155. doi:10.1186/S12920-018-0460-9/TABLES/5
- 763 46. El Hassouni B, Mantini G, Immordino B, Peters GJ, Giovannetti E. CX-5461 Inhibits
764 Pancreatic Ductal Adenocarcinoma Cell Growth, Migration and Induces DNA Dam-
765 age. *Molecules* 2019, Vol 24, Page 4445. 2019;24(24):4445. doi:10.3390/MOLE-
766 CULES24244445
- 767 47. Xu H, di Antonio M, McKinney S, et al. CX-5461 is a DNA G-quadruplex stabilizer
768 with selective lethality in BRCA1/2 deficient tumours. *Nature Communications* 2017
769 8:1. 2017;8(1):1-18. doi:10.1038/ncomms14432

Figure Legends

Figure 1. rRNA 2'Ome levels vary in high-grade adult-type diffuse gliomas. An unsupervised hierarchical clustering of C-scores at the 106 known rRNA 2'O-ribose methylated (2'Ome) sites was performed in a test cohort of 40 high-grade (3-4) adult-type diffuse glioma (HGG) samples and 6 non-tumoral, non-neoplastic cerebral cortex (NT) samples. C-scores are represented by a color scale from 0 (black) to 1 (yellow). IDHwt glioblastomas (G), high-grade astrocytomas (A), high-grade oligodendrogliomas (O) and non-neoplastic (NT) samples are depicted in pink, green, purple, and grey, respectively. The mean C-score for each site across the 46 samples is shown on the right-hand side of the graph. 86 sites have a mean C-score higher than 0.9 (black) and 20 sites lower than 0.9 (red).

Figure 2. The most variable rRNA 2'Ome sites are sufficient to distinguish different HGG types. (A) Distribution of the interquartile range (IQR) of the C-score to determine the C-score variability across HGG samples of the test cohort (n=40). rRNA 2'Ome sites are ranked by increasing IQR value. The IQR distribution curve is plotted at the right-hand side of the graph. The "most variable sites" correspond to those with an IQR higher than median + 2 × median absolute deviation (mad) and were colored in red (19 sites). (B-D) Unsupervised Principal Component Analysis (PCA) based on C-scores of the 19 most variable sites as identified in (A). Independent PCA was performed on IDHwt glioblastoma (G, pink circle), high-grade astrocytoma (A, green triangle) and high-grade oligodendroglioma (O, purple diamond) samples of both test (B, n=40) and validation (n=23) cohorts. Validation cohort samples were projected on PCA of the test cohort (D). Percentage of variance explained by PC1 and PC2 are indicated. 95 % confidence ellipsoids around the centroid of each group (larger pink circle, green triangle and purple diamond) are indicated.

Figure 3. rRNA 2'Ome levels are differently altered in HGG types. (A) Box plots showing the distribution of C-score in HGG and non-neoplastic samples of the test cohort for 16 rRNA 2'O-ribose methylated (2'Ome) sites that exhibited both statistically and biologically significant alterations between groups. These sites were identified using both Kruskal-Wallis statistical tests (with an adjusted p-value threshold of < 0.05)

and a mean $\Delta C\text{-score}_{\text{max-min}} > 0.05$ (absolute difference between the highest and lowest mean C-score). The adjusted p-values corresponding to the statistical tests are indicated on the bottom left-hand side of each panel and median C-scores are represented by a black line within the box plots. **(B)** Pairwise comparison of mean C-score groups for the 16 significantly deregulated rRNA 2'Ome sites in the test cohort. Positive (UP) and negative (DOWN) $\Delta C\text{-score}_{\text{group1-group2}}$ are shown in blue and red, respectively. Adjusted p-values: *: $p < 0.05$; **: $p < 0.01$; ***: $p < 0.001$; ****: $p < 0.0001$; ns, not significant.

Figure 4. Expression profiles of RiBi factors distinguish HGG types. **(A)** Panel of genes involved in ribosome biogenesis constituting the 20 RiBi-gene set analyzed in HGG and non-neoplastic samples. Genes located on the short arm of chromosome 1 (1p) or long arm of chromosome 19 (19q), which are heterozygously deleted in high-grade oligodendrogliomas, are indicated. **(B)** A principal component analysis (PCA) based on the mRNA expression profile of the RiBi-gene set. Each dot represents a non-neoplastic (NT, grey square), IDHwt glioblastoma (G, pink circle), high-grade astrocytoma (A, green triangle) or high-grade oligodendroglioma (O, purple diamond) sample. Ellipsoids shows 90% confidence interval around the centroid (larger grey square, pink circle, green triangle, and purple diamond) of each group. Percentage of variance explained by PC1 and PC2 are indicated. **(C)** A heatmap showing Pearson's correlation coefficients of PC1 to PC5 axes with the overall survival (OS), progression-free survival (PFS) and mitotic index. R-values are depicted by different colors from -0.6 (red, negative correlation) to 0.6 (blue, positive correlation). Significant correlations are indicated by an asterisk: ** $p < 0.01$; *** $p < 0.001$.

Figure 5. High-grade astrocytomas and oligodendrogliomas display the highest increased expression in ribosome biogenesis factors. Box plots showing relative mRNA expression levels determined by RT-qPCR analysis of the RiBi genes implicated in rRNA **(A)** transcription and **(B)** maturation, **(C)** snoRNA biogenesis or associated to **(D)** H/ACA box and **(E)** C/D box snoRNAs in IDHwt glioblastomas (G, pink), high-grade astrocytomas (A, green), high-grade oligodendrogliomas (O, purple) and non-neoplastic (NT, grey) samples. *FBL*, *PIH1D1* and *RUVBL2* are located on chromosomes 1p or 19q.

Figure 6. Glioma spheroids reveal distinct histomolecular type-dependent sensitivity to ribosome biogenesis inhibitors. **(A)** Representative high-content screening microscopy images of 5706, N131520, BT138, BT237 and LGG85 cell line spheroids treated or not (DMSO) with 10 μ M of BMH-21 for 72 h. Hoechst and CellTox labelling are depicted in blue and green, respectively. Cell lines representative of glioblastomas, high-grade oligodendrogliomas and astrocytomas are shown in pink, purple and green, respectively. **(B)** Representative graphs indicating the viability percentage in response to increasing BMH-21 concentrations in 5706, N131520, BT138, BT237 and LGG85 cell line spheroids. Cell lines representative of IDHwt glioblastomas, IDHmut oligodendrogliomas and astrocytomas are framed in pink, purple and green, respectively. **(C)** A table indicating means and standard deviations (SD) of BMH-21 IC₅₀ calculated from graphs displayed in (B) (n=7). (D), (E) and (F) as in (A) (B) and (C), respectively, for CX5461 (n=3).

Table 1. Clinical characteristics of patients with high-grade primary diffuse gliomas constituting the test cohort

	Glioblastoma (n=13)	Astrocytoma grade 3/4 (n=13)	Oligodendroglioma grade 3 (n=14)
Age (years) mean [min-max]	60 [52-73]	36 [25-52]	53 [35-66]
Gender			
Female	4 (31%)	4 (31%)	5 (36%)
Male	9 (69%)	9 (69%)	9 (64%)
Tumor location			
Temporal	3 (23.1%)	3 (23.1%)	2 (14.3%)
Frontal	7 (53.8 %)	10 (76.9%)	12 (85.7%)
Occipital	1 (7.7%)	0 (0%)	0 (0%)
Parietal	2 (15.4%)	0 (0%)	0 (0%)
Genetic alteration			
mutation <i>IDH1/2</i>	0 (0%)	13 (100%)	14 (100%)
del 1p/19q	0 (0%)	0 (0%)	14 (100%)
ATRX-	NA	12 (92.3%)	0 (0%)
Progression			
Yes	12 (92.3%)	5 (38.5%)	3 (21.4%)
No	0 (0%)	8 (61.5%)	11 (78.6%)
NA	1 (7.7%)	0 (0%)	0 (0%)
Tumor cells (%) mean [min-max]	55 [30-85]	38 [20-60]	40 [20-70]

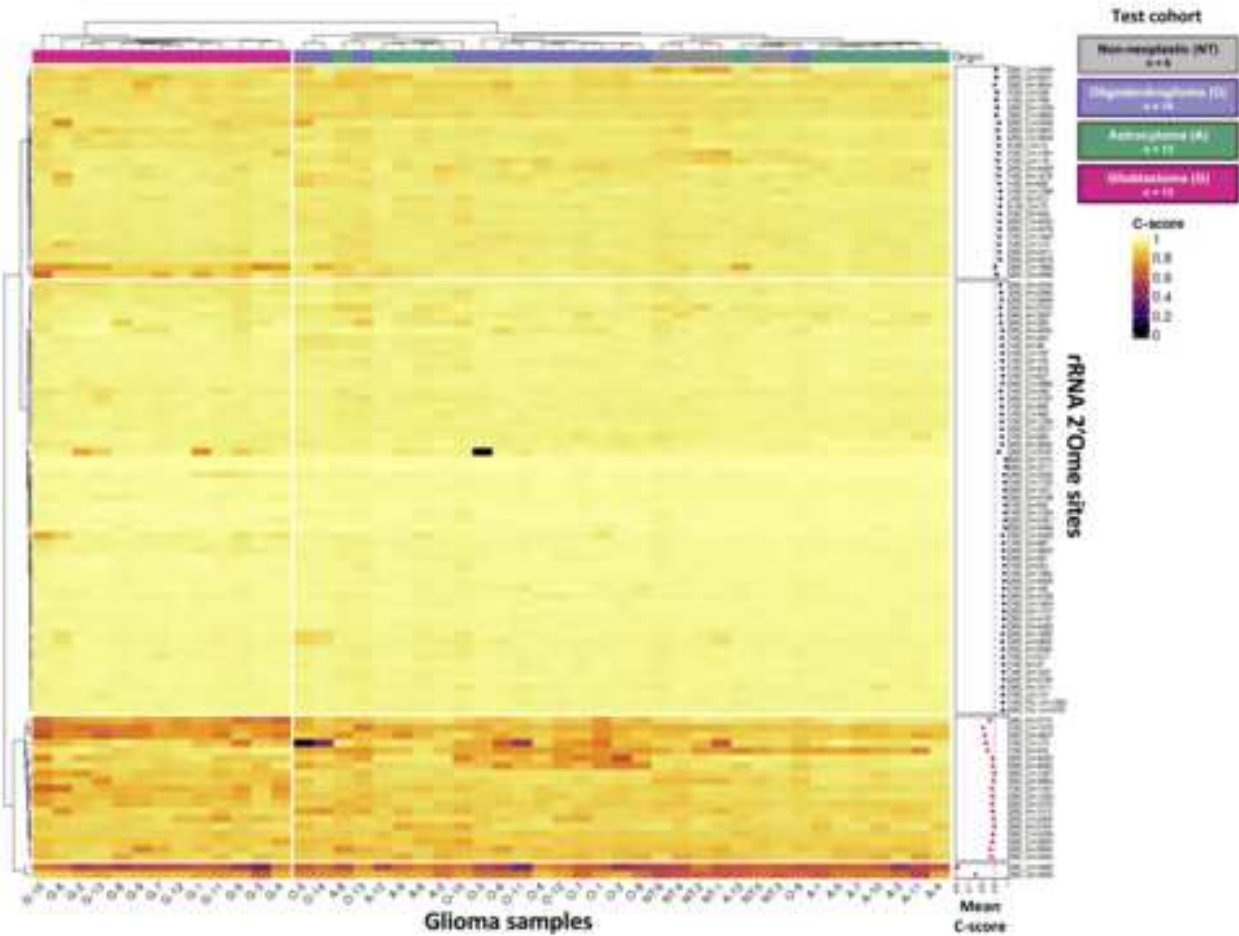


Figure 1



Figure 2

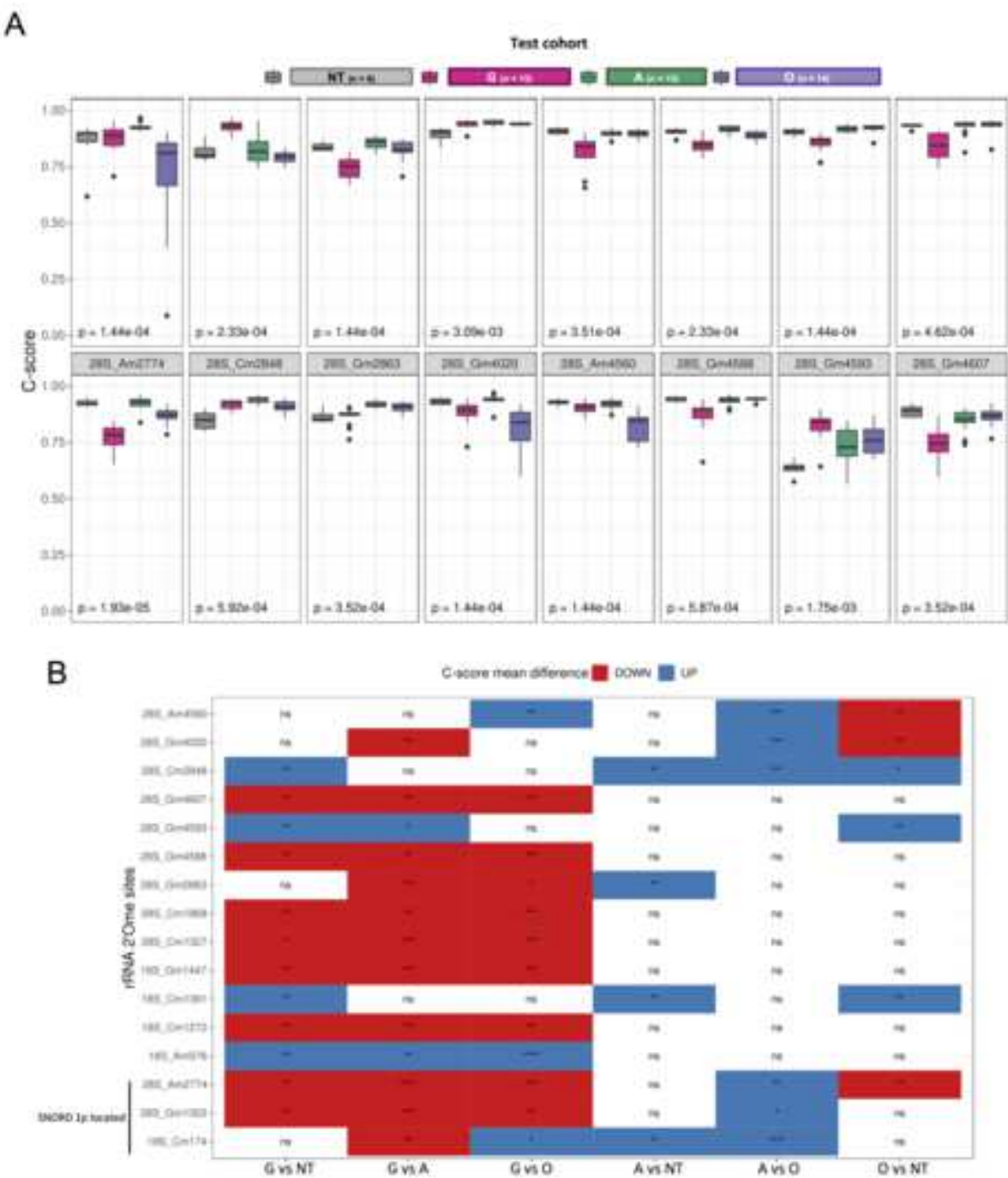


Figure 3

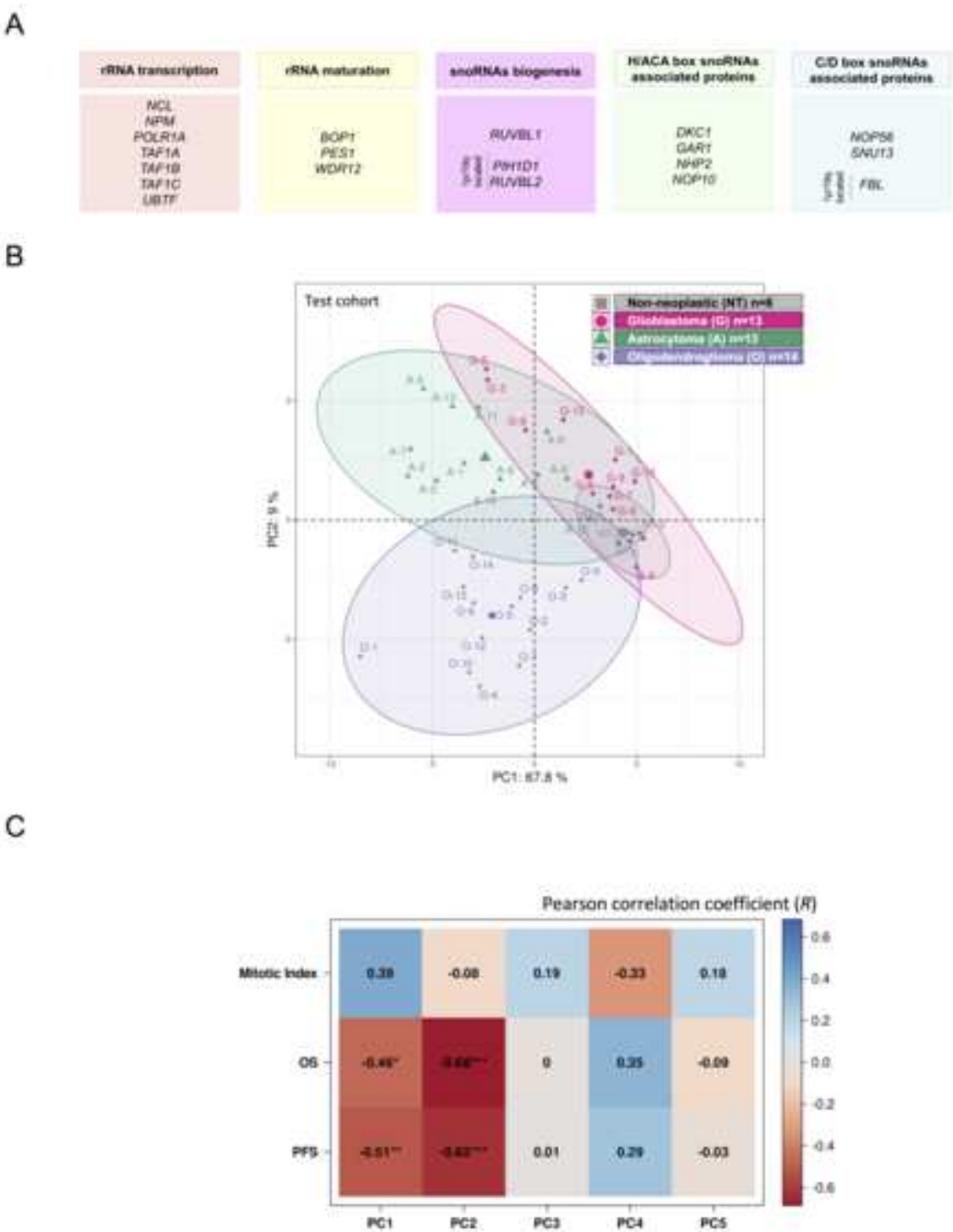


Figure 4

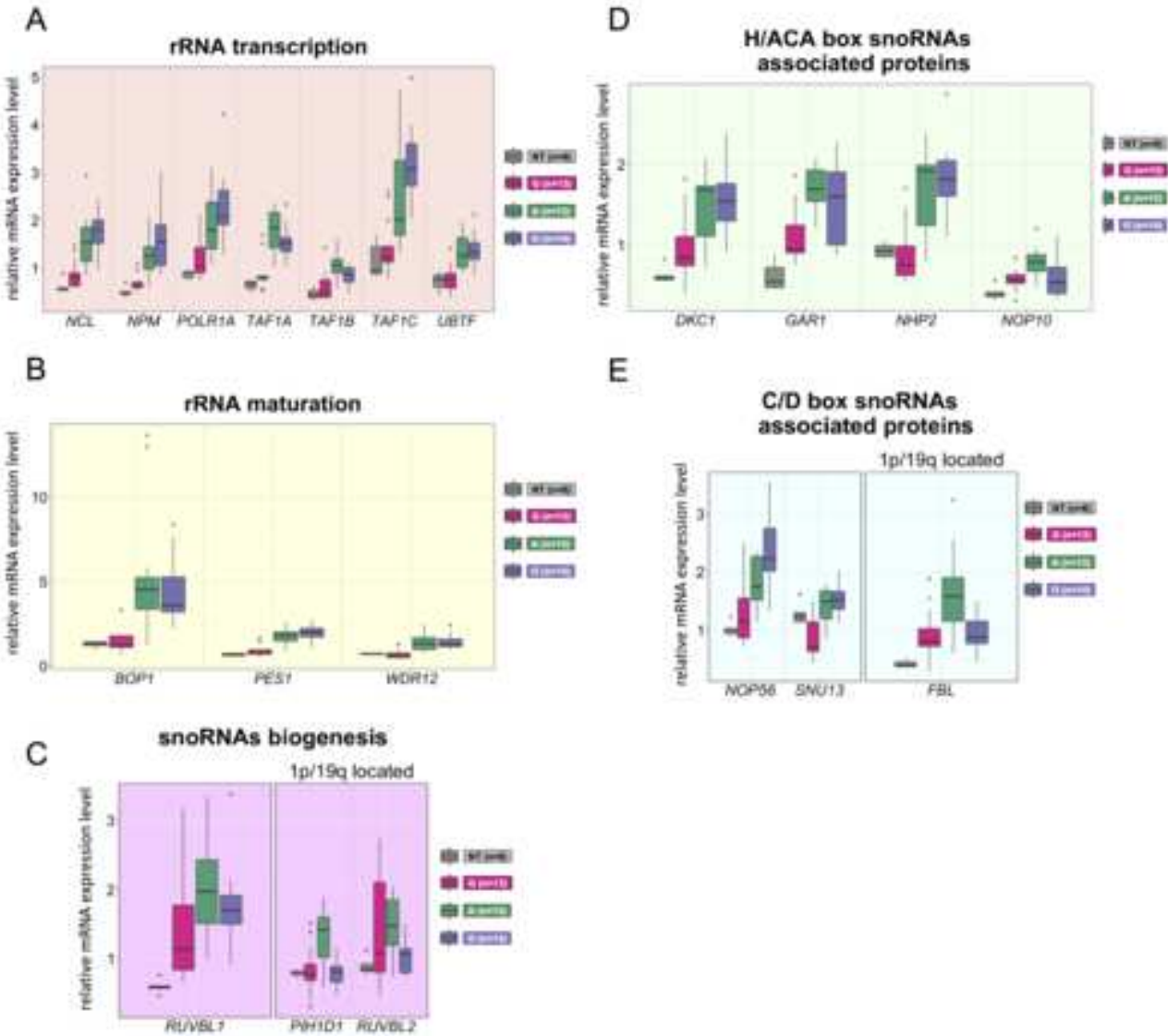


Figure 5

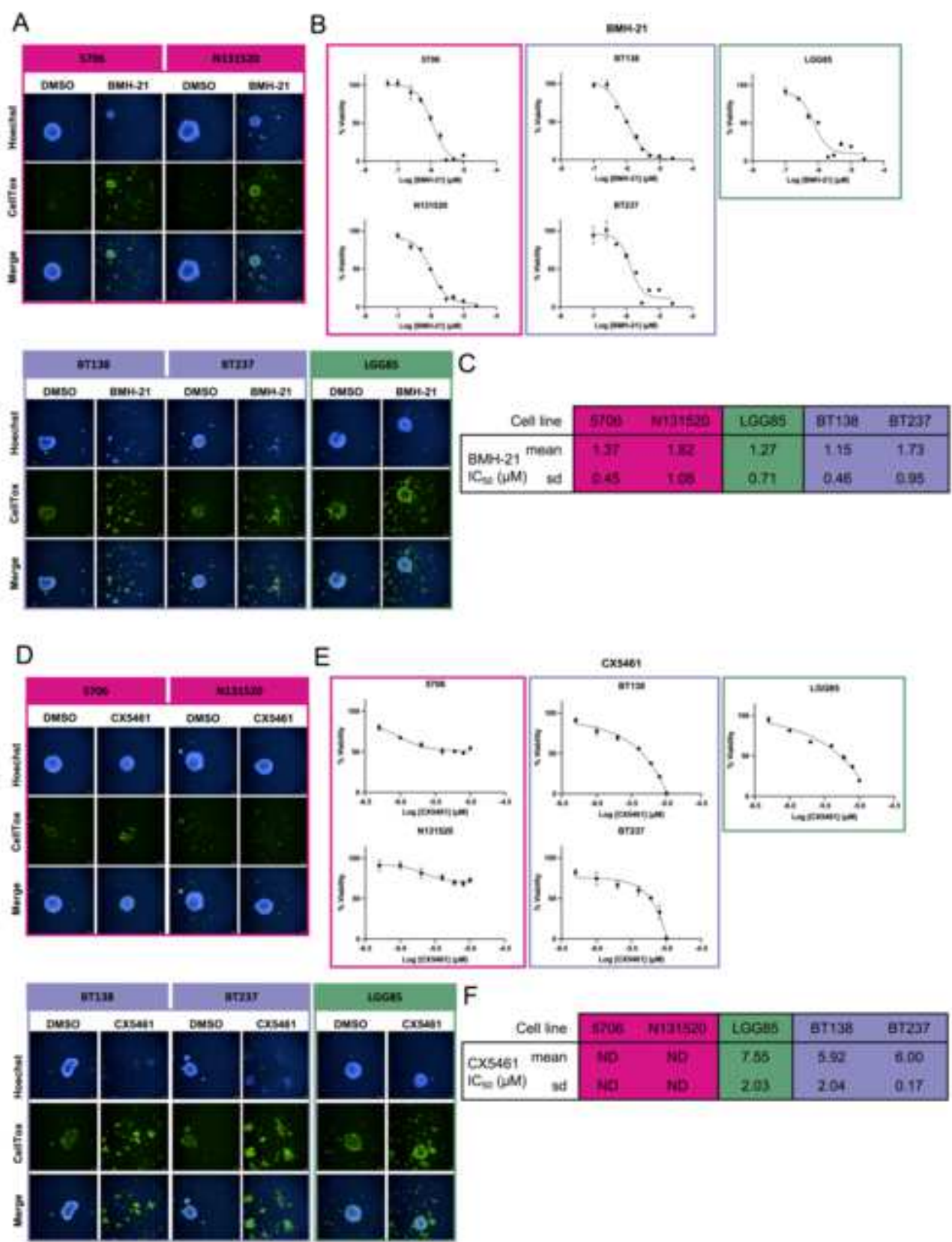
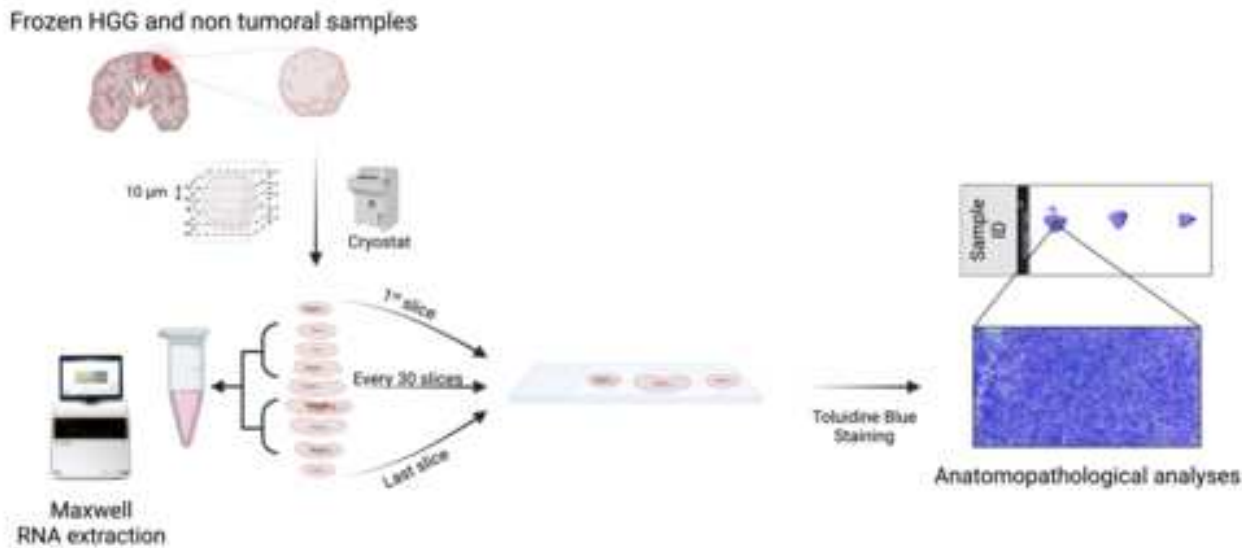


Figure 6

A



B

Test Cohort			Validation Cohort		
	Sample ID	% tumoral cells		Sample ID	% tumoral cells
Oligodendrogliomas	O-1	60	Glioblastomas	G-1	30
	O-2	40		G-2	80
	O-3	20		G-3	50
	O-4	50		G-4	60
	O-5	20		G-5	40
	O-6	40		G-6	65
	O-7	60		G-7	60
	O-8	50		G-8	70
	O-9	20		G-9	30
	O-10	50		G-10	50
	O-11	20		G-11	30
	O-12	30		G-12	70
	O-13	70		G-13	70
	O-14	20			
Astrocytomas	A-1	20	Oligodendrogliomas	O-a	70
	A-2	20		O-b	90
	A-3	30		O-c	80
	A-4	30		O-d	80
	A-5	20		O-e	40
	A-6	60		O-f	60
	A-7	30		O-g	90
	A-8	40		O-h	40
	A-9	60	Astrocytomas	A-a	30
	A-10	30		A-b	20
	A-11	40		A-c	20
	A-12	60		A-d	30
	A-13	50		A-e	80
				A-f	50
			Glioblastomas	G-a	50
				G-b	60
				G-c	70
				G-d	80
				G-e	40
				G-f	70
				G-g	70
				G-h	30
				G-i	60

Figure S1

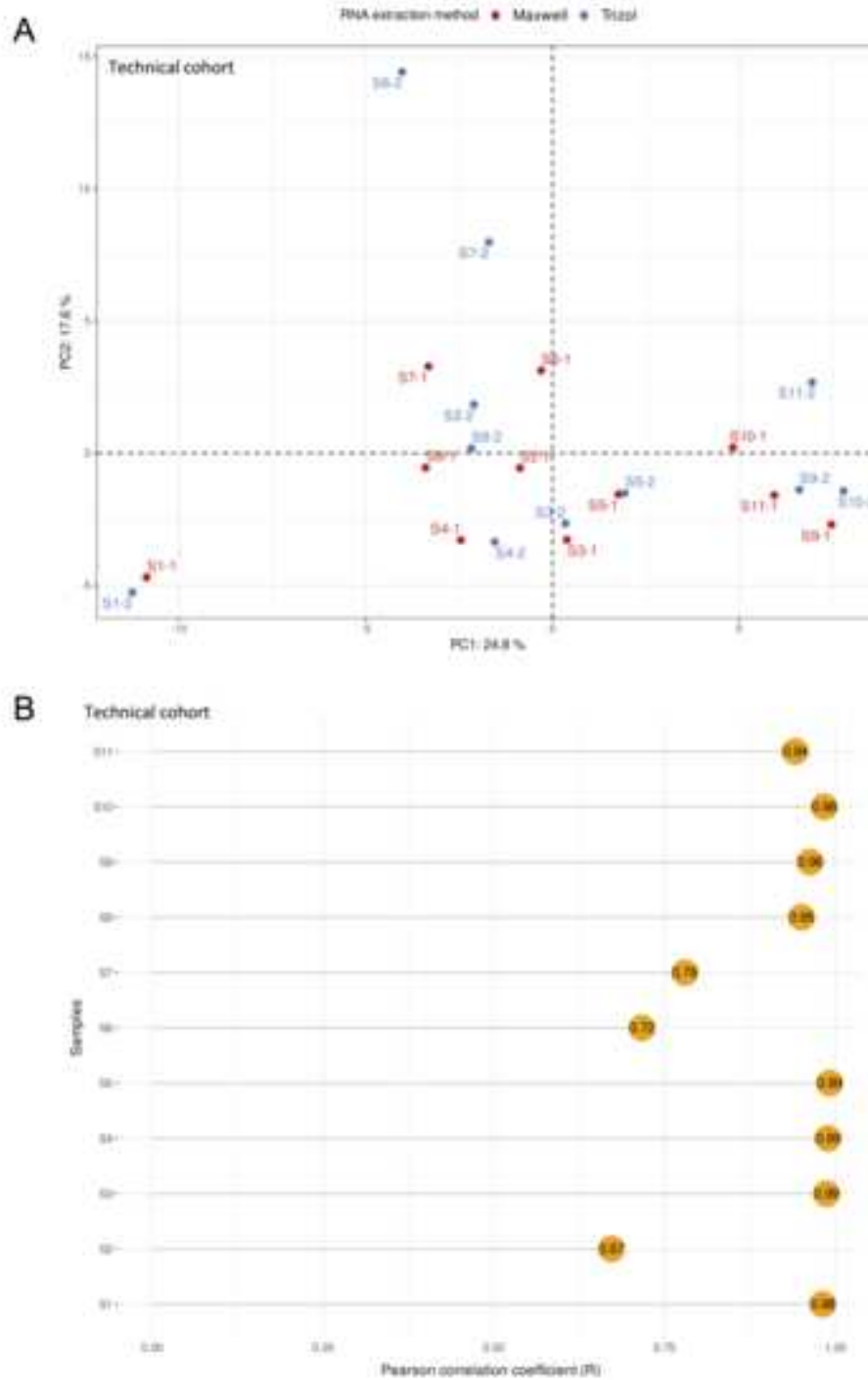


Figure S2

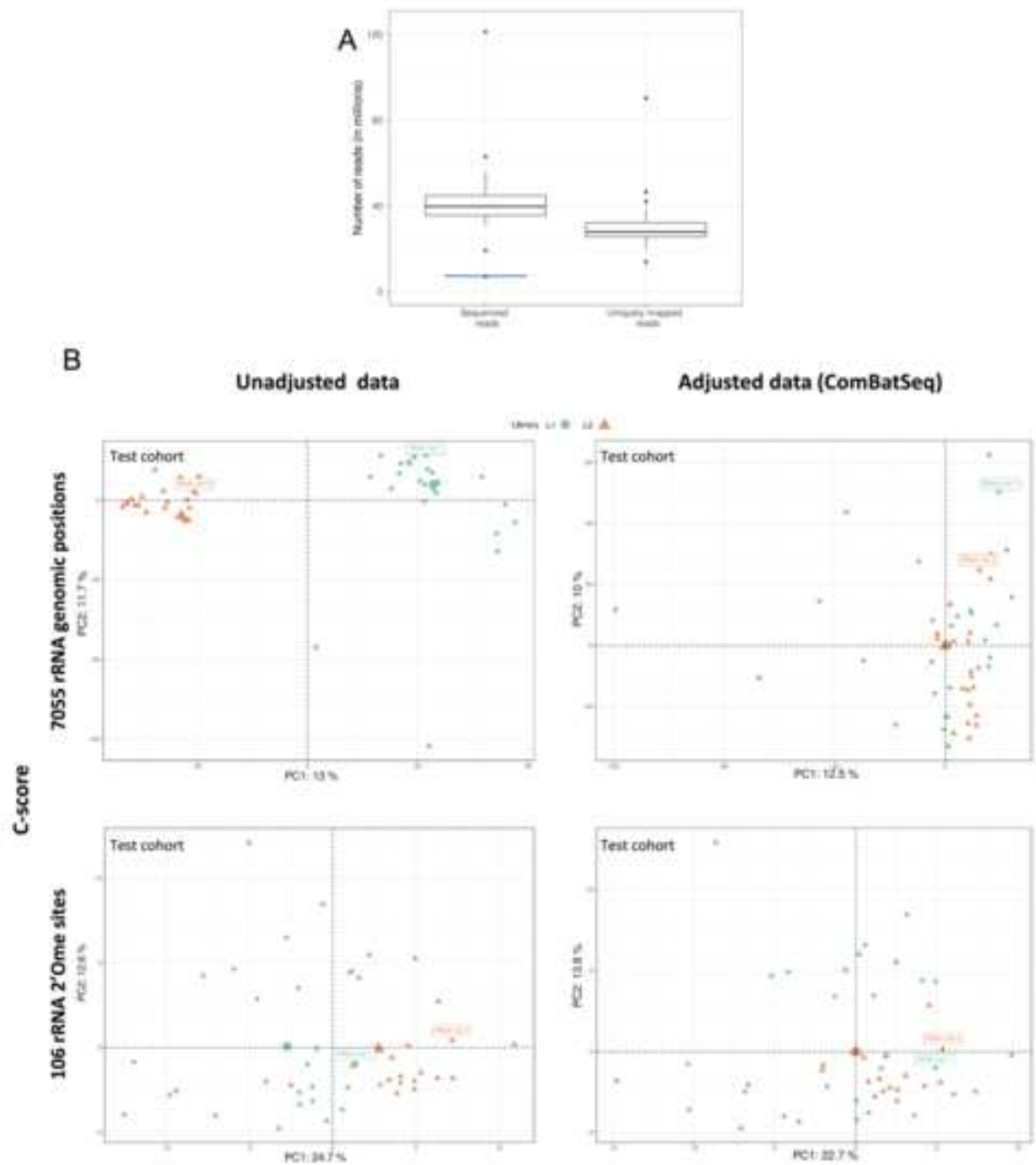


Figure S3

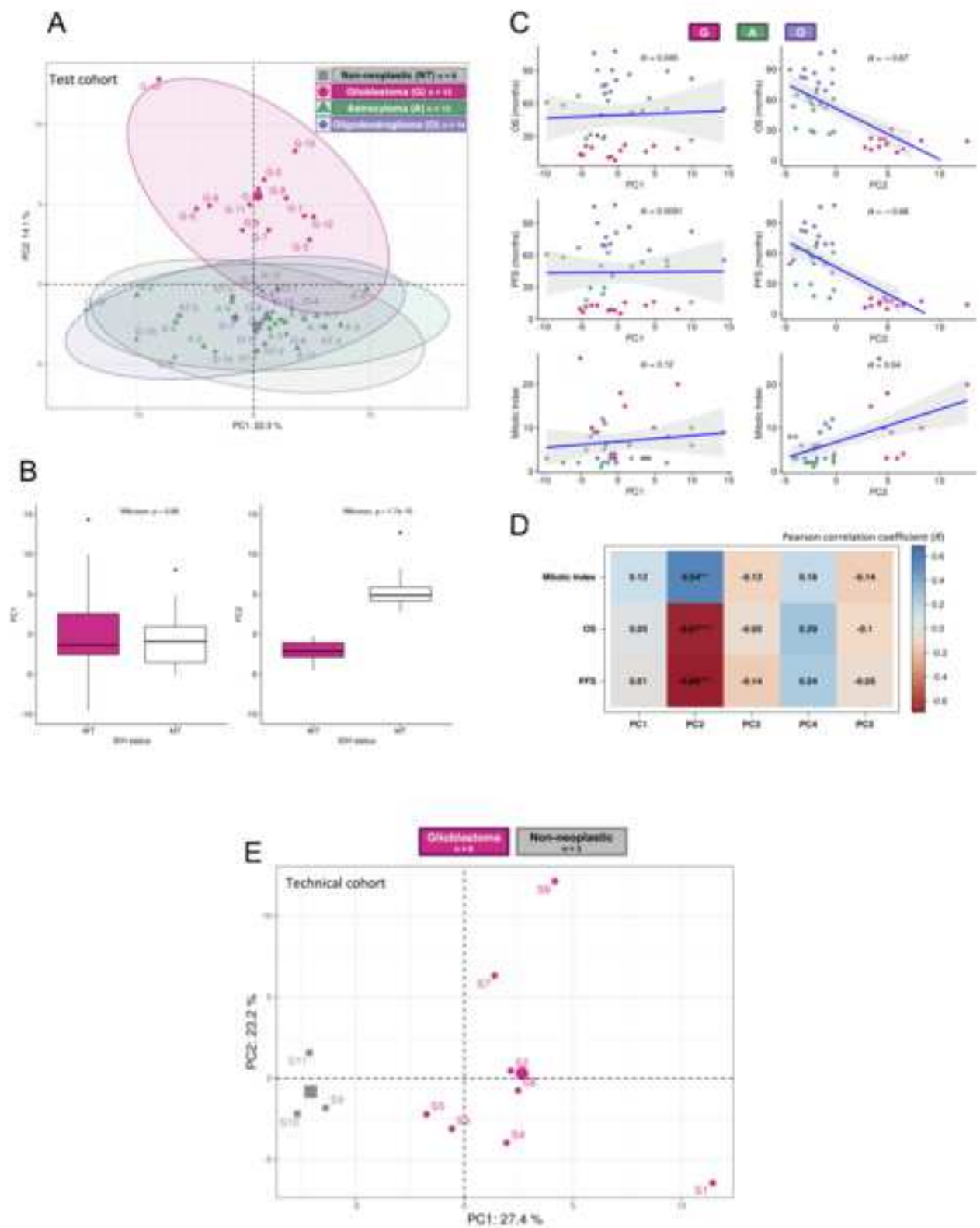


Figure S4

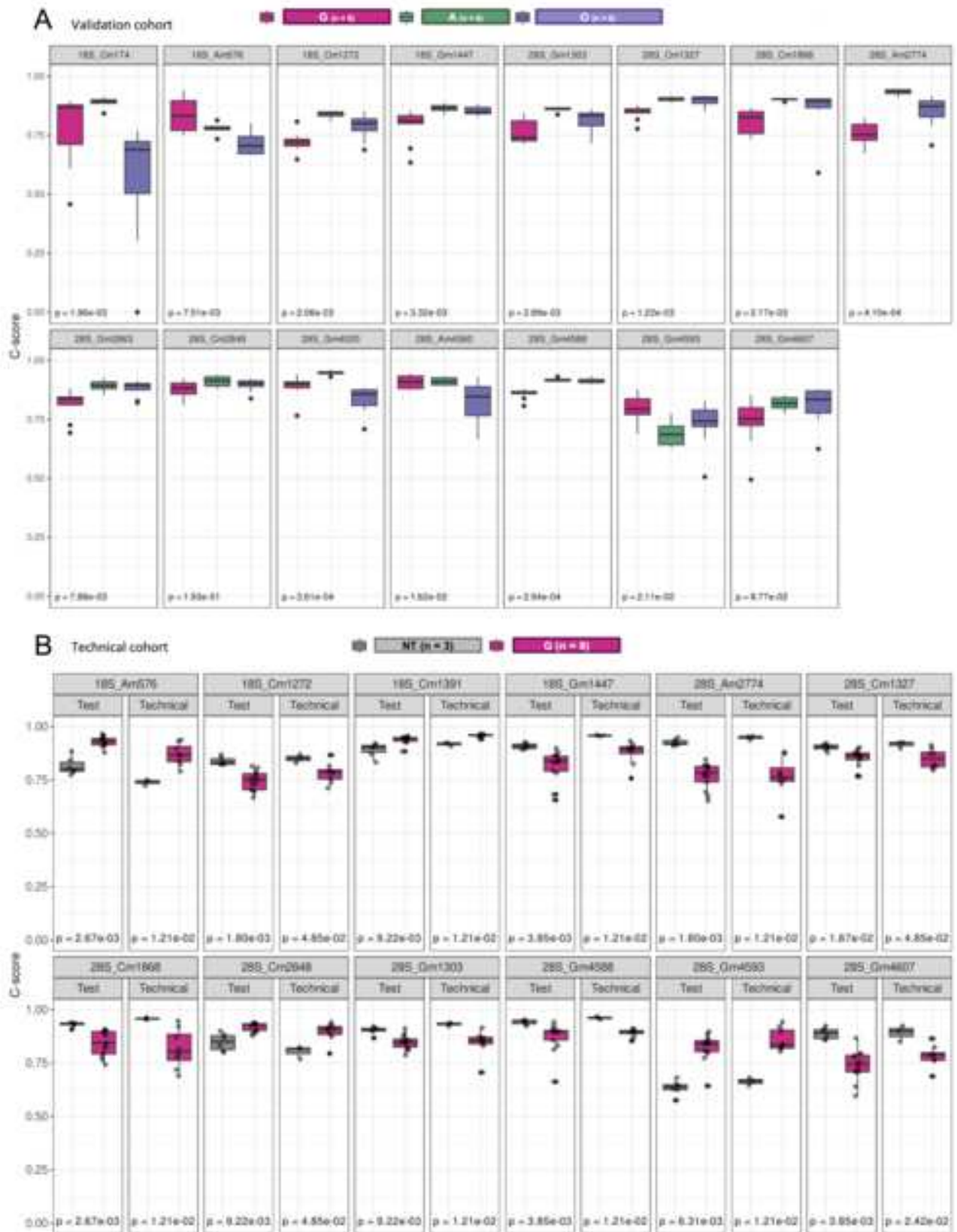


Figure S5

Figure S6

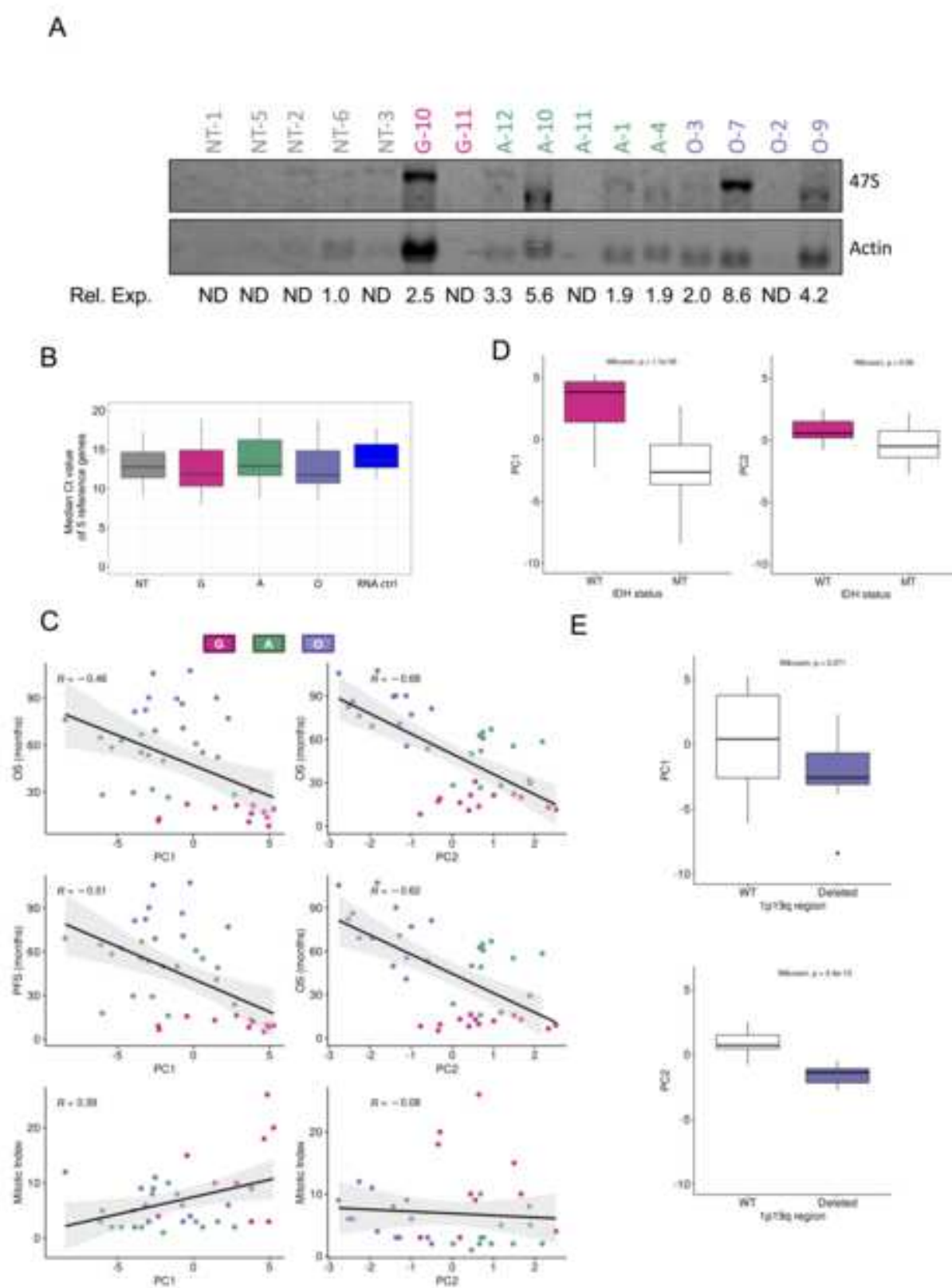


Figure S7

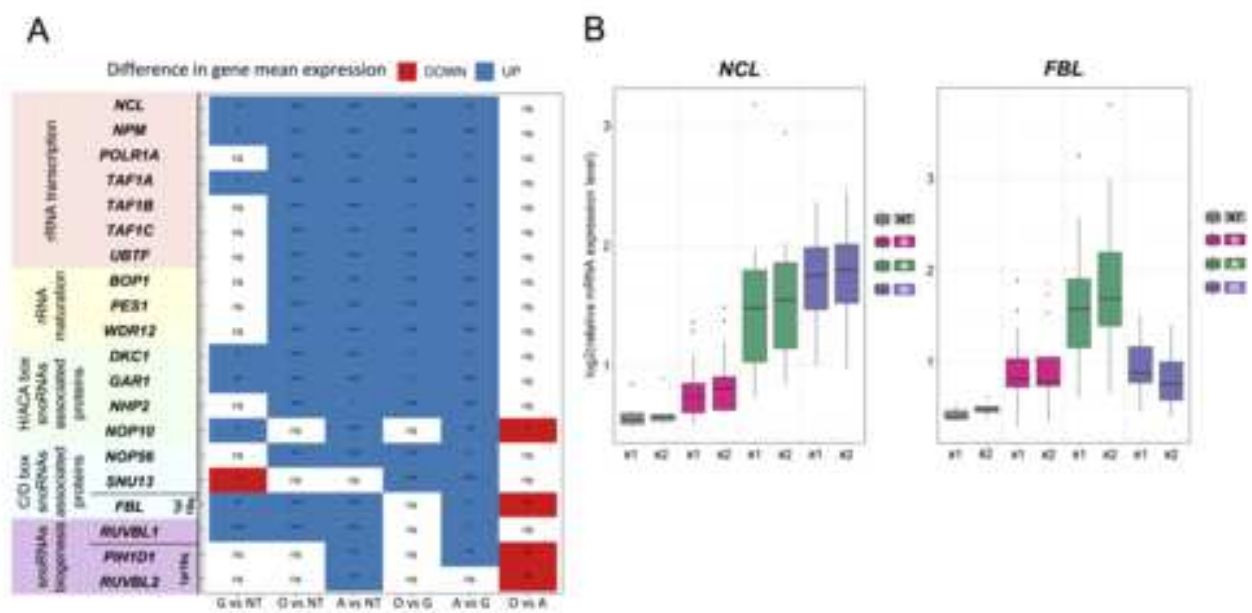


Figure S8

Supplementary Information

IDHwt and IDHmut adult-type diffuse gliomas display distinct alterations in ribosome biogenesis and 2'O-methylation of ribosomal RNA

Hermes PARAQINDES^{1,2,#}, Nour-EI-Houda MOURKSI^{1,#}, Samantha BALLESTA^{1,3,#}, Jordan HEDJAM¹, Fleur BOURDELAIS^{1,4}, Tanguy FENOUIL^{1,9}, Thiébaud PICART^{1,9}, Frédéric CATEZ¹, Théo COMBE^{1,2}, Anthony FERRARI^{1,2}, Janice KIELBASSA², Emilie THOMAS^{1,2}, Laurie TONON^{1,2}, Alain VIARI^{1,2,5}, Valéry ATTIGNON^{1,6}, Marjorie CARRERE^{1,6}, Jessie PERROSSIER^{1,6}, Stéphane GIRAUD^{1,3}, Christophe VANBELLE^{1,12}, Mathieu GABUT¹, Danny BERGERON⁷, Michelle S SCOTT⁷, Luis CASTRO VEGA⁸, Nathalie MAGNE⁸, Emmanuelle HUILLARD⁸, Marc SANSON⁸, David MEYRONET^{1,9}, Jean-Jacques DIAZ¹, François DUCRAY^{1,11,*}, Virginie MARCEL^{1,#,*}, Sébastien DURAND^{1,#,*}

1. LabEx Dev2CAN, Institut Convergence Plascan, Centre de Recherche en Cancérologie de Lyon, Inserm U1052, CNRS UMR5286, Université de Lyon, Université Claude Bernard Lyon 1, Centre Léon Bérard, CEDEX 08, F-69373 Lyon, France

2. Synergie Lyon Cancer, Gilles Thomas Bioinformatics Platform, Centre Léon Bérard, CEDEX 08, F-69373 Lyon, France

3. Plateforme organoïdes 3D-ONCO, Université de Lyon, Université Claude Bernard Lyon 1, Inserm U1052, CNRS UMR5286, Centre Léon Bérard, Centre de Recherche en Cancérologie de Lyon (CRCL), Lyon, 69373, France

4. Inovaron, 75005, Paris, France.

5. INRIA Grenoble Rhône-Alpes, 38330 Montbonnot-Saint-Martin, France

6. Cancer Genomics Platform, Centre de Recherche en Cancérologie de Lyon, CEDEX 08, F-69373 Lyon, France

7. Département de biochimie et génomique fonctionnelle, Faculté de médecine et des sciences de la santé, Université de Sherbrooke, Sherbrooke, Québec J1E 4K8, Canada

8. Sorbonne Université, Inserm, CNRS, UMRS1127, Institut du Cerveau, ICM, AP-HP, Hôpitaux Universitaires La Pitié Salpêtrière – Charles Foix, Service de Neurologie 2-Mazarin, 75013 Paris, France

35 9. Hospices Civils de Lyon, Laboratoire de biologie médicale et d'anatomie
36 pathologique
37 10. Hospices Civils de Lyon, Service de Neurochirurgie tumorale et vasculaire, Hôpital
38 Pierre Wertheimer
39 11. Hospices Civils de Lyon, Service de neuro-oncologie, Hôpital Pierre Wertheimer
40 12. Plateforme d'Imagerie Cellulaire, Université de Lyon, Université Claude Bernard
41 Lyon 1, Inserm U1052, CNRS UMR5286, Centre Léon Bérard, Centre de Recherche
42 en Cancérologie de Lyon (CRCL), Lyon, 69373, France
43
44 # Equal contribution as co-first or co-last authors
45 * Corresponding authors: francois.ducray@chu-lyon.fr,
46 virginie.marcel@lyon.unicancer.fr and sebastien.durand@inserm.fr

Supplementary Materials and Methods

Cell culture

Human IDHwt glioblastoma 5706 and N131520 (from Dr A Idbaih), IDHmut astrocytoma LGG85 (from Dr JP Hugnot), and IDHmut and 1p/19q codeleted oligodendroglioma BT138 and BT237 (from Dr K Ligon) cell lines were cultured as spheres in Ultra Low Attachment 6-well plates (Dutscher) to inhibit cell adhesion and promote sphere formation. Spheroids were passaged at most 30 times by enzymatic dissociation (Accumax, Sigma-Aldrich,). Glioblastoma and astrocytoma spheroids were cultured in DMEM/F12 medium (Gibco) supplemented with 1X B27 and 1X N2 supplement (Fisher Scientific), 20 ng/mL bFGF (Miltenyi), 20 ng/mL EGF (Miltenyi) and 1X Penicillin/Streptomycin (Gibco). Oligodendroglioma spheroids were cultured in NeuroCult NS-A Proliferation medium (STEMCELL technologies) supplemented with 20 ng/mL bFGF, 20 ng/mL EGF and 1X Penicillin/Streptomycin.

Human grade 3-4 adult-type diffuse glioma and non-neoplastic samples

Three cohorts were build using tumoral and non-neoplastic samples collected between 2010-2016 (NeuroBioTec, CRB HCL, Lyon, France, Biobank BB-0033-00046). First, a technical cohort containing 11 samples, including 8 grade 4 IDHwt glioblastoma (G) and 3 non-tumoral (NT) samples (epilepsy surgery), was selected. Second, a test cohort was composed of 40 high-grade (3-4) primary adult-type diffuse glioma samples and comprised 13 IDHwt glioblastomas (G, annotated G1 to G13), 13 IDHmut astrocytomas (grade 3 n=9, grade 4 n=4) (A, A1 to A13) and 14 IDHmut and 1p/19q codeleted oligodendrogliomas (grade 3) (O, A1 to A14) (WHO 2021 classification) (Table 1). Six non-tumoral (NT) control samples were provided by patients without diagnosed brain neoplastic events between 2003-2015 (epilepsy surgery for tuberous sclerosis complex n=3 or for other cause n=2, autopsy n=1). Finally, a validation cohort was composed of 23 high-grade (3-4) gliomas, including 9 IDHwt glioblastomas (G, annotated Ga to Gi), 6 IDHmut astrocytomas (grade 3 n=5, grade 4 n=1) (A, Aa to Af) and 8 IDHmut and 1p/19q co-deleted oligodendrogliomas (grade 3) (O, Oa to Oh). The percentage of tumoral cells was estimated by a neuropathologist using Carboic Toluidine Blue staining (RAL Diagnostics) during RNA preparation (Fig.S1). HGGs were classified using an integrated histomolecular algorithm according to WHO 2021

classification, e.g., IDH-R132H immunostaining followed by *IDH1/2* targeted Next Generation Sequencing. In the test cohort, tumor samples were associated with clinical data, including the *IDH1/2* mutational status, the mitotic index and patient survival (Table 1). Overall survival (OS) was defined as the survival duration from the date of surgery (biopsy or surgery) to either the date of death or last follow-up. Progression-free survival (PFS) corresponded to the survival duration from the date of surgery (biopsy or surgery) to either the date of radiological tumor progression, death, or last follow-up. Patients were informed and written consent of all participants was obtained in accordance with French regulations.

Sample preparation and RNA purification

Approximately 15 to 30 frozen 10 µm sections were cut on a cryostat (Leica Biosystems CM3050S) (Supplementary Figure S1A). The first, last and every 30th section of each sample were stained with Carboic Toluidine Blue (RAL Diagnostics) to assess sample homogeneity and, when required, to estimate the percentage of tumoral cells before RNA purification (Supplementary Figure S1B). Total RNA was extracted using either the Maxwell RSC simplyRNA Tissue Kit (Promega) on a Maxwell RSC Instrument (Promega) configured with Low Elution Volume (LEV) hardware according to the manufacturer's protocol or TRIzol (Invitrogen) according to manufacturer's instructions. RNA quality and concentrations were measured using a Nanodrop 2000 Spectrophotometer (ThermoScientific).

RiboMethSeq

RiboMeth-seq was performed as previously described using the Illumina sequencing technology^{25,32}. Briefly, total RNA was fragmented under alkaline conditions prior to the preparation of 24 sample libraries using the NEBNext Multiplex Small RNA Library kit (New England Biolabs). A calibrated source of total RNA (Human Xpress Ref Universal Total RNA, Qiagen) was introduced in each library. In contrast to previous studies, sequencing was performed using an Illumina NovaSeq sequencer in single-end mode (SR50), in order to sequence up to 48 samples (equivalent to 2 libraries) per run with a median sequencing depth of 40 million reads per sample.

To process the sequencing data, a novel nextflow pipeline RiboMethSeq-nf was developed and is currently available (<https://github.com/RibosomeCRCL/ribomethseq-nf>). This pipeline processes sequencing data as previously described^{25,32,33}. Briefly,

fastQC was used to verify sequencing quality and adapter removal was performed using Trimmomatic. The trimmed reads were aligned by Bowtie2 on the 7.2 kb-long rRNA sequence of reference (NR_046235) and the 5' read-ends were computed using bedtool genomcov utility. To calculate the C-score, which reflects the rRNA 2'Ome level, the novel R package rRMSAnalyzer was developed (<https://github.com/RibosomeCRCL/rRMSAnalyzer>). The C-score was calculated using a normalization against the median raw counts of neighboring +/- 6 nucleotide window²⁵.

The C-scores of the 106 admitted rRNA 2'Ome sites were extracted for further analysis, either as a rRNA 2'Ome profile or as a site-by-site comparison. The most variable rRNA 2'Ome sites were identified using the distribution of the inter quartile range (IQR) of each site across the test cohort samples²⁵, the sites having an IQR higher than median + 2 × median absolute deviation (mad) being defined as the most variable ones. The identification of significant alterations in rRNA 2'Ome levels between groups was performed by applying two consecutive thresholds: the adjusted p-value < 0.05 (Kruskal-Wallis with FDR adjustment); and the mean Δ C-score (*i.e.*, difference between the highest and lowest mean C-score of the groups of interest) > 0.05.

Batch effect adjustment of RiboMethSeq data using ComBat-Seq

Batch effect adjustment of RiboMethSeq data was performed using 5' read-end count matrix as input for ComBat-seq¹. As currently reported for RNA-seq data, a batch effect between two libraries may be observed using RiboMethSeq. ComBat-seq tool was developed to adjust batch effect in RNA-seq data following a negative binomial distribution and both its input and output are integer counts. ComBat-seq was used with default parameter settings. This process produces an adjusted 5' read-end count matrix that is then used to calculate the C-score as described above. Adjustment of RiboMethSeq data using ComBat-seq has been included in the rRMSAnalyser R package as an optional function (<https://github.com/RibosomeCRCL/rRMSAnalyzer>).

Reverse Transcription and real time quantitative PCR

cDNA synthesis was performed using the Prime Script RT Reagent kit (Takara) from 500 ng or 200 ng of total RNA for real time and medium throughput qPCR, respectively. Gene expression was evaluated by medium throughput qPCR using the Biomark HD

system (Fluidigm), as previously described²¹, and according to the manufacturer's instructions. For each sample, two independent reverse transcription reactions were performed. A PCR multiplex was first carried out to amplify genes of interest and facilitate their detection (Table S1). After exonuclease I treatment, qPCR reactions were performed on a 96.96 Dynamic Array™ IFC (Fluidigm) using the Master Mix 2X EvaGreen (Biorad) according to manufacturer's recommendations, in technical triplicates. The Fluidigm Real Time PCR Analysis software (v 4.5.2) was used for the calculation of relative fold-changes by applying the $2^{-\Delta CT}$ method based on a total of 6 Ct values per sample. The median Ct value of 5 housekeeping mRNAs (*ACTIN*, *GAPDH*, *HPRT1*, *PGK1*, *PPIA*) was used for normalization. Data were then normalized against Human Xpress Ref Universal Total RNA (Qiagen) as a standard RNA. Real time qPCR was performed using SYBR Green (Roche, Applied Biosystem) according to the manufacturer's protocol. Serial dilutions were systematically included to calculate qPCR efficacy, verify amplification linearity, and calculate relative cDNA concentrations. Relative fold-change was calculated as described above using *PPIA* mRNA levels to normalize SNORD levels.

Northern blot

RNA samples were analyzed by northern blot as previously described². Briefly, total RNAs were resolved by electrophoresis on 1.2% agarose, 6% formaldehyde, 0.02 M 3-(*N*-morpholino)propanesulfonic acid (MOPS) gels. Transfers were performed by capillarity on a nylon membrane (Nytran SuperCharge, Whatman) with 10X SSC (1.5 M sodium chloride, 0.15 M sodium citrate, pH 7.0). Membranes were incubated overnight at 42°C with hybridization buffer (ULTRAhyb™-Oligo, Invitrogen) containing Dy682-conjugated human β -actin (10 nM) and Dy782-conjugated 47S pre-rRNA (50 nM) DNA probes. Membranes were washed four times with 0.1X SSC and 0.1% SDS before signal exposure on ChemiDoc MP (Bio-Rad). Quantification was performed using Image Lab software (Bio-Rad) and relative 47S pre-rRNA levels were determined by normalization against β -actin mRNA levels.

β -actin probe 1: 5'-Dy682-TTGACATGCCGGAGCCGTTGTCGACGAC-3'

β -actin probe 2: 5'-Dy682-CACACGCAGCTCATTGTAGAAGGTGTGGTGCC-3'

β -actin probe 3 5'-Dy682-CGTACATGGCTGGGGTGTGAAGGTCTCAAACAT-3'

47S ribosomal RNA probe:

5'-Dy782-

CGGAGGCCCAACCTCTCCGACGACAGGTCGCCAGAGGACAGCGTGTTCAGC-3'

snoRNA quantification using RiboMethSeq data

SnoRNAs were quantified from RiboMethSeq datasets as previously described ³. Briefly, Trimmomatic was used to remove adaptors and low-quality reads ⁴. Trimmed reads were aligned with STAR ⁵ to the human genome assembly (Ensembl hg38 V101) using our custom annotation (based on Ensembl hg38 V101) containing added snoRNAs

(https://zenodo.org/record/4570182/files/hg38_Ensembl_V101_Scottlab_2020.gtf) ⁶.

Counts were attributed to genomic features using CoCo ⁷ and our custom annotation.

IC₅₀ assay

Approximately 3.10^3 cells per well were seeded onto 96-well microplates Ultra Low Attachment (Corning, 4515) in triplicate to form spheroids. After overnight incubation, spheroids were treated with seven or nine doses of CX5461 (Sigma-Aldrich)²⁴ or BMH-21 (Sigma-Aldrich)²⁵, respectively, at constant final DMSO concentrations (1%). After 72 h, cell cytotoxicity was assessed by CellToxTM Green Cytotoxicity Assay (Promega), according to the manufacturer's instructions, followed by imaging using Opera Phoenix[®] Plus High-Content Screening System, and by CellTiter-Glo3D[®] luminescent cell viability assay (Promega) quantified with Spark[®] microplate to determine the IC₅₀. Cell viability was expressed as a percentage of the signal intensity normalized against DMSO (1%).

Statistical methods

Data and statistical analyses of both RT-qPCR and RiboMethSeq as well as graphical representation, were performed using R (v 4.1.2). Unsupervised data analysis was achieved by hierarchical clustering and principal component analysis (PCA). Hierarchical clustering was generated with the ComplexHeatmap package using Manhattan distance and Ward's linkage method. PCA was computed using ade4 package with the default parameters and visualized via factoextra package. To correlate the first 5 principal components (PCs) of the PCA on gene expression or rRNA 2'Ome profiles with the clinical features (OS, PFS, mitotic index), the

eigencorplot function of PCAtools package was used. Pearson's correlation coefficient and the False Discovery Rate (FDR) method for the adjusted p-values were applied. Pairwise comparison between groups was performed using non-parametric Wilcoxon rank-sum test, or Kruskal-Wallis test when more than 2 groups were identified. The FDR method was used for p-value adjustment when multiple tests were undertaken. A p-value < 0.05 was considered to be statistically significant. Regarding the rRNA 2'Ome, in addition to a significant adjusted p-value, a mean Δ C-score greater than 0.05 was considered for identifying differentially methylated 2'Ome rRNA 2'Ome sites, the Δ C-score corresponding to the difference between the highest and the lowest mean C-score of the groups of interest. Cell viability and IC₅₀ were determined using the log(inhibitor) vs. response variable slope sigmoidal (four PL) function of GraphPad Prism (v 9.5.0 (525)).

Supplementary References

1. Zhang Y, Parmigiani G, Johnson WE. ComBat-seq: batch effect adjustment for RNA-seq count data. *NAR Genom Bioinform.* 2020;2(3). doi:10.1093/NARGAB/LQAA078
2. Durand S, Franks TM, Lykke-Andersen J. Hyperphosphorylation amplifies UPF1 activity to resolve stalls in nonsense-mediated mRNA decay. *Nature Communications* 2016 7:1. 2016;7(1):1-12. doi:10.1038/ncomms12434
3. Fafard-Couture É, Bergeron D, Couture S, Abou-Elela S, Scott MS. Annotation of snoRNA abundance across human tissues reveals complex snoRNA-host gene relationships. *Genome Biol.* 2021;22(1):1-24. doi:10.1186/S13059-021-02391-2/FIGURES/6
4. Bolger AM, Lohse M, Usadel B. Trimmomatic: a flexible trimmer for Illumina sequence data. *Bioinformatics.* 2014;30(15):2114-2120. doi:10.1093/BIOINFORMATICS/BTU170
5. Dobin A, Davis CA, Schlesinger F, et al. STAR: ultrafast universal RNA-seq aligner. *Bioinformatics.* 2013;29(1):15-21. doi:10.1093/BIOINFORMATICS/BTS635
6. Bergeron D, Laforest C, Carpentier S, et al. SnoRNA copy regulation affects family size, genomic location and family abundance levels. *BMC Genomics.* 2021;22(1). doi:10.1186/S12864-021-07757-1
7. Deschamps-Francoeur G, Boivin V, Abou Elela S, Scott MS. CoCo: RNA-seq read assignment correction for nested genes and multimapped reads. *Bioinformatics.* 2019;35(23):5039-5047. doi:10.1093/BIOINFORMATICS/BTZ433

258 **Supplementary Table 1. RT-qPCR primer sequences**

Genes	Forward primer	Reverse primer	Genomic location
<i>*Actin</i>	5'-CCAACCGCGAGAAGATGA-3'	5'-TCCATCACGATGCCAGTG-3'	7p22.1
<i>BOP1</i>	5'-GACGATCCTGACTACTGGCG-3'	5'-ACCTGCTCATCCGTCAGTCT-3'	8q24.3
<i>DKC1</i>	5'-CCCTTTGGAAAAGCTGTTGA-3'	5'-TAATCTTGGCCCCATAGCAG-3'	Xq28
<i>FBL #1</i>	5'-CCTGGGGAATCAGTTTATGG-3'	5'-CCAGGCTCGGTACTCAATTTT-3'	19q13.2
<i>FBL #2</i>	5'-CCTGCGTAATGGAGGACACT-3'	5'-GCTGAGGCTGTGGAGTCAAT-3'	
<i>*GAPDH</i>	5'-AGCCACATCGCTCAGACAC-3'	5'-GCCCAATACGACCAAATCC-3'	12p13.31
<i>GAR1</i>	5'-CAAGACCAAGGACCTCCAGA-3'	5'-TCATCTTCACAGGGATGCAG-3'	4q25
<i>*HPRT1</i>	5'-TGACACTGGCAAAACAATGCA-3'	5'-GGTCCTTTTACCAGCAAGCT-3'	Xq26.2
<i>NCL #1</i>	5'-CCAGAACCAAAATGGCAAAT-3'	5'-CTGATTGCTCTGCCCTCAAT-3'	2q37.1
<i>NCL #2</i>	5'-GTCAGCAAGGATGGGAAAAG-3'	5'-TAGATCGCCCATCGATCTCT-3'	
<i>NHP2</i>	5'-GGTCAACCAGAACCCCATC-3'	5'-TTCTGCTTCACCGCTTTCTT-3'	5q35.3
<i>NOP10</i>	5'-GAAGAAATTTGACCCGATGG-3'	5'-TGAAGCGTTTCTTGATGGTG-3'	15q14
<i>NOP56</i>	5'-AGGCTATTCTGGATGCCTCA-3'	5'-GTAGGCTCTGGCGGTATTCA-3'	20p13
<i>NPM</i>	5'-TTGTTGAAGCAGAGGCAATG-3'	5'-TATTTCAAAGCCCCCAAGG-3'	5q35.1
<i>PES1</i>	5'-GGCAAGAGGCGAAAAATCCG-3'	5'-TTCTTCTCAGACCTCACCGC-3'	22q12.2
<i>*PGK1</i>	5'-AAGTGAAGCTCGGAAAGCTTCTAT-3'	5'-AGGGAAAAGATGCTTCTGGG-3'	Xq21.1
<i>PIH1D1</i>	5'-TGAGTCTGGGAGAGCCTCAT-3'	5'-AAATCGCTGTTCTGCATCCT-3'	19q13.33
<i>POLR1A</i>	5'-CTGAGCCCCTGGGAATTGAG-3'	5'-CCTTCATTCTTCCACAGGGCA-3'	2p11.2
<i>*PPIA</i>	5'-GTCAACCCACCGTGTTCTT-3'	5'-CTGCTGTCTTTGGGACCTTGT-3'	7p13
<i>RUVBL1</i>	5'-AAGGGGATGTGC ACA AAA AG	5'-CACATCCAAGTCATGCAAGG-3'	3q21.3
<i>RUVBL2</i>	5'-CGCTCTTCTCAGGTGACACA-3'	5'-CAGCACTCCAGGGATGATCT-3'	19q13.33
<i>SNU13</i>	5'-GCTACTGGACCTCGTTCAGC-3'	5'-ACTCAGAGATGCCCTGTTG-3'	22q13.2
<i>TAF1A</i>	5'-TCCTGGAGTTTGGGACCCTT-3'	5'-TGGTGAGTACCTCTTGGGCT-3'	1q41
<i>TAF1B</i>	5'-CGAGGAGGCGGAAGAGTTTA-3'	5'-TCTCTCTGTAACATTGTGGCAAGA-3'	2p25.1
<i>TAF1C</i>	5'-CGGAGTGAAGATGCTGGACA-3'	5'-GCCCCCAAACGAAAAAGCAA-3'	16q24.1
<i>UBTF</i>	5'-TGTGGAACGACCTGTCTGAG-3'	5'-CTCTCCGACTGAGCCTTGAG-3'	17q21.31
<i>WDR12</i>	5'-TAAAGGGGCAGAGGAATGGAT-3'	5'-CAACATCCGTATGTCCCACAA-3'	2q33.2
<i>SNORD31</i>	5'- ACCAGTGATGAGTTGAATACCG-3'	5'- CACAGCTCAGAAAATACCTTTCA-3'	11q12.3
<i>SNORD104</i>	5'-GCCTGCTGTGATGACATTCC-3'	5'-TCAGACTCCAGTTCGCATCA-3'	17q23.3
<i>SNORD144</i>	5'-TTCATATCCAGTGATTAAACCTTTTC-3'	5'-ATTCAATAATCACAACGGTTCA-3'	4q21.22
<i>SNORD127</i>	5'-GCAACTGTGATGAAAGATTTGGT-3'	5'-GGCAACATCAGTTTAGAGGGA-3'	14q21.2
<i>SNORD46</i>	5'-AGAATCCTTAGGCGTGGTTG-3'	5'-ATGACAAGTCCTTGCAATTGG-3'	1p34.1
<i>SNORD93</i>	5'-GCCAAGGATGAGAACTCTAATCTGA-3'	5'-GCCTCAGGTAAATCCTTTAATCCA-3'	7p15.3
<i>SNORD69</i>	5'-TGAAGCAAATGATGATAAACTGG-3'	5'-AACATGAAGCTCAGGGTTGG-3'	3p21.1
<i>SNORD119</i>	5'-AACCTTGACTGAAGCTGATGA-3'	5'-CTGGATCTCAGAGTAATCCTGCT-3'	20p13
<i>SNORD65</i>	5'-AAATCACCCAAAATAGCTGGAA-3'	5'-TCAGAAAACCATAGGTTACCA-3'	17p11.2
<i>SNORD91A</i>	5'-CGTCTGAACCTGTCTGAAGCA-3'	5'-GGAGAAGTCTCAGAACCACACA-3'	17p13.3
<i>SNORD91B</i>	5'-AGAGCCAATGATGTTTTTATTCAA-3'	5'-ACACAGAAGTTGCATCACTGG-3'	17p13.3
<i>SNORD80</i>	5'-ACAATGATGATAACATAGTTCAGCAG-3'	5'-ATCAGATAGGAGCGAAAGACTTAATA-3'	1q25.1

259 **Housekeeping genes*

260

Supplementary Figure Legends

Figure S1. Sample processing and anatomopathological analyses. (A) Diagram presenting the workflow of sample processing. Briefly, snap frozen tissues of the test and validation cohorts were cut into 10 μm -slices using a cryostat. The first, the last as well as one slice every 30 sections were placed on glass slides and stained with Toluidine Blue for analysis by an anatomopathologist to estimate the number of slices required for further analyses, to verify the tumor integrity in the course of tumor cutting and to collect tumoral features (percentage of tumoral cells, necrosis). Other slices were pooled and RNA extraction was performed on a Maxwell® apparatus. For the technical cohort, pooled slices were separated in half and RNA was extracted using either Trizol or Maxwell®. Created with Biorender.com. **(B)** A table indicating the percentage of tumor cells in each sample from the test and the validation cohorts.

Figure S2. Reproducibility of RiboMethSeq using two different methods of RNA extraction. (A) An unsupervised Principal Component Analysis (PCA) based on C-scores of the 106 known rRNA 2'Ome sites of the technical cohort composed of 11 samples. Total RNA was extracted either by Maxwell (S1-1 to S11-1, red) or Trizol (S1-2 to S11-2, blue) methods. Percentage of variance explained by PC1 and PC2 are indicated. **(B)** Summary of Pearson's correlation coefficient (R) of C-scores obtained with the two different RNA extraction methods. In the technical cohort, a strong correlation between C-scores was observed within the same sample, regardless of the method used for RNA purification.

Figure S3. RiboMethSeq optimization using Illumina NovaSeq device and ComBat-seq algorithm. (A) Distribution of the numbers of either sequence reads or uniquely mapped reads using the Illumina NovaSeq device in the 48 samples of the test cohort (40 HGGs, 6 non-neoplastic and 2 reference RNAs). A blue line indicates the mean of sequence reads obtained in a previous work using an Illumina HiSeq device (Marcel et al. NAR cancer 2021). **(B)** Unsupervised Principal Component Analysis (PCA) based on either C-scores at 7055 rRNA sites (top) or C-scores at the 106 known rRNA 2'Ome sites (bottom) before (left) and after (right) adjustment of 5'-

end read counts using ComBat-seq algorithm. The 48 samples of the test cohort were prepared as two distinct libraries (L1, green; L2, red). RNA control samples included in each library are indicated.

Figure S4. IDHwt glioblastomas have a distinct rRNA 2'Ome profile, which is correlated with clinical features. (A) Unsupervised Principal Component Analysis (PCA) on adjusted C-scores at the 106 known rRNA 2'Ome sites in the test cohort composed of IDHwt glioblastoma (G, pink circle), high-grade astrocytoma (A, green triangle), high-grade oligodendroglioma (O, purple diamond) and non-neoplastic (NT, grey square) samples. Percentage of variance explained by PC1 and PC2 are indicated. The 95 % confidence ellipsoids around the centroid (larger pink circle, green triangle, purple diamond and grey square) of each group are drawn. (B) Box plots showing the distribution of IDHwt and IDHmut HGG samples of the test cohort on PC1 (left panel) or PC2 (right panel) axes. P-values using non-parametric Wilcoxon rank-sum test are indicated on top. (C) Correlations between the clinical features (OS: overall survival; PFS: progression-free survival; and mitotic index) and projections on either PC1 (left) and PC2 (right) are displayed for the HGG types of the test cohort. Pearson's correlation coefficients (R) are indicated on top. (D) A heatmap showing Pearson's correlation coefficients (R), as calculated in (C), of PC1 to PC5 axes with sample clinical features for the test cohort. R values are depicted by different colors from -0.6 (red, negative correlation) to 0.6 (blue, positive correlation). Significant correlations are indicated by an asterisk: ** $p < 0.01$; *** $p < 0.001$. (E) Unsupervised PCA based on the C-score of the 106 known rRNA 2'Ome sites of the technical cohort composed of 3 non-neoplastic (grey square) and 8 IDHwt glioblastoma (pink circle) samples.

Figure S5. Comparison of rRNA 2'Ome sites significantly altered between HGG subtypes (A) or glioblastoma and non-neoplastic samples (B) in independent cohorts. Box plots showing the C-score distribution in HGG subtypes of the validation cohort (A) or in IDHwt glioblastoma (pink) and non-neoplastic (grey) samples of the technical cohort (B) for the 15 and 12 sites identified in the test cohort shown in Figure 3, respectively. P-values determined by Kruskal-Wallis or Mann-Whitney statistical

tests are indicated at the bottom of each panel and median C-scores are drawn as black lines.

Figure S6. Comparison of rRNA 2'Ome levels and expression of related C/D box snoRNAs. (A) Correlations of the expression of 12 C/D box snoRNAs (SNORDs) in a panel of 9 HGG samples of the test cohort either determined from RiboMethSeq data (TPM, y-axis) or measured by RT-qPCR (relative mRNA expression, x-axis). Spearman's correlation coefficients (R) are indicated with corresponding p-values. (B) Summary of Spearman's correlation coefficient (R) between C-scores at 46 rRNA sites and associated-SNORD expressions both determined by RiboMethSeq in the test cohort. The most variable sites identified in Figure 2 are indicated. Significant correlations are indicated with asterisk: * $p < 0.05$; ** $p < 0.01$; *** $p < 0.001$; **** $p < 0.0001$. (C) Correlation of C-scores at 18S_Am576 and corresponding expression levels of the related SNORD93 in the test cohort. R and p-value are indicated on the top left-hand side of the graph.

Figure S7. HGG histomolecular types display IDH mutational status-associated disparities in RiBi. (A) Northern blots using probes targeting the 47S pre-rRNA and actin mRNAs on IDHwt glioblastoma (G, pink), high-grade astrocytoma (A, green), high-grade oligodendroglioma (O, purple) and non-neoplastic (NT, grey) samples. The 47S pre-rRNA expression is normalized against actin mRNA signals and expression levels depending on "NT-6" samples are indicated below ("Rel. Exp"). ND: 47S pre-rRNA expression levels could not be determined due to undetectable actin mRNA levels. (B) Distribution of median Ct values of 5 reference genes (*ACTIN*, *GAPDH*, *HPRT1*, *PGK1*, *PPIA*) in the HGG subtypes of the test cohort: IDHwt glioblastomas (G, pink); high-grade astrocytomas (A, green); high-grade oligodendrogliomas (O, purple); non-neoplastic (NT, grey) samples; and a reference RNA (RNA ctrl, blue) (C) Correlation between the clinical features (OS: overall survival; PFS: progression-free survival; and mitotic index) of HGG samples and projections on either PC1 (left) or PC2 (right) axes from PCA in Figure 4B. Pearson's correlation coefficients (R) are indicated on top left-hand side. Each dot corresponds to a sample colored as in (B). (D) Distribution of IDHwt and IDHmut HGG samples on PC1 (left panel) or PC2 (right panel) axes from PCA in Figure 4B. P-values using non-parametric Wilcoxon rank-sum

test are indicated on top. **(E)** Distribution of 1p19q deleted or non-deleted ("WT") samples on PC1 (top panel) or PC2 (bottom panel) axes from PCA in Figure 4B. P-values using non-parametric Wilcoxon rank-sum test are indicated on top.

Figure S8. RiBi is elevated in high-grade astrocytomas and oligodendrogliomas.

(A) Summary of pairwise comparisons of relative mRNA expression levels of individual RiBi genes from the RiBi-gene set. Positive and negative fold-changes are shown in blue and red, respectively. Adjusted p-value using Wilcoxon Mann Whitney statistical test are indicated (*: $p < 0.05$; **: $p < 0.01$; ***: $p < 0.001$; ****: $p < 0.0001$; ns, not significant). Genes located in the region 1p/19q are indicated. **(B)** Relative expression of *NCL* (left) and *FBL* (right) mRNAs in IDHwt glioblastoma (G, pink), high-grade astrocytomas (A, green), high-grade oligodendrogliomas (O, purple), non-neoplastic (NT, grey) samples determined by RT-qPCR using 2 different primer sets (#1 and #2).